analytical chemistry

pubs.acs.org/ac Article

Polarized Distribution of Lipid Droplets with Long Acyl Chains and Unsaturation are Hallmarks of Human Intestinal Enteroid Differentiation

Patrik K. Johansson,[§] Yueming Liu,[§] Katarina C. Klett, Sarah C. Heilshorn,* and Annika Enejder*

Cite This: *Anal. Chem.* 2025, 97, 27076−27090 Read Online

ACCESS | Metrics & More | Article Recommendations | Supporting Information

ABSTRACT: Cell polarization and differentiation require increased energy mobilization and cell membrane synthesis, whereby mitochondria and lipid droplets (LDs) play key roles. However, how these metabolic organelles organize at the subcellular level to efficiently meet energy demands in human intestinal organoids is unclear. To address this, we introduce coherent anti-Stokes Raman scattering (CARS) microscopy multiplexed with confocal fluorescence microscopy to spatially map LDs and mitochondria throughout cell differentiation in human intestinal enteroids. The results show an overall decrease in LDs over time, though less pronounced for cells positive for proliferation or stemness markers. The LD depletion was observed in the apical region, resulting in a polarized distribution to the basal side. A similar mitochondrial polarization pattern was also observed in differentiated enteroids. Spectral CARS further shows that LDs postdifferentiation contain lipids with signatures of longer acyl chains and a higher degree of unsaturation. These observations demonstrate that polarized metabolic and lipid supply infrastructures are formed to support intestinal cell differentiation in organoid cultures.

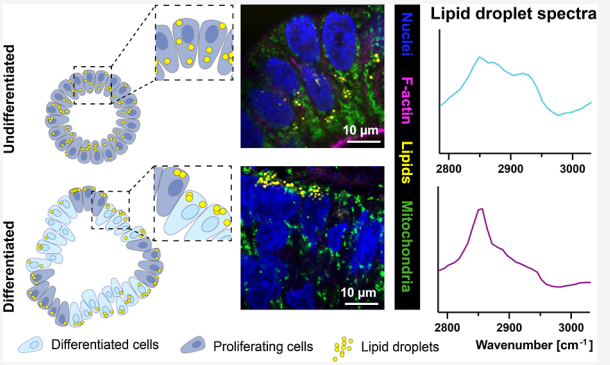

INTRODUCTION

Intestinal organoids have emerged as powerful model systems replicating important characteristics of the intestine, including self-renewal capacity, multilineage differentiation, barrier integrity, and polarized absorption.[1−6] While intestinal stem cell (ISC) location, proliferation profiles, and differentiation trajectories are still being defined in tissue,[7−15] ISCs can be traced over time in organoids, offering a tractable system to study the fundamental mechanisms underlying stem cell renewal and differentiation, tissue development, and regeneration.[1,2,16,17] Further, intestinal organoids derived from human cells provide human-relevant insights into nutrient and drug uptake studies and hold great promise for studying gut−microbiome interactions[4,18−26] and disease progression.[27,28] In addition, they have been successfully applied for use in in vitro expansion of patient-derived stem cells and as transplants for stem cell delivery in regenerative therapy of digestive diseases.[27,29−32] For all these fundamental studies and clinically relevant applications, information on and control of the metabolic status of the organoid and its spectrum of stem to differentiated cells is crucial.

To date, most studies of intestinal cell metabolism have been performed on murine intestinal tissues and organoids. Bmi1-expressing stem cells in murine tissue and undifferentiated organoids rely mainly on glycolysis without significant mitochondrial respiration,[33] similar to multiple other adult stem cell types.[34−38] In contrast, upon differentiation of murine intestinal organoids, the Lgr5$^+$ stem cells found in crypt-like formations show increased mitochondrial oxidation[33,39,40] fueled by lactate from the adjacent Paneth cells,[33] which rely on glycolysis. However, Lgr5$^+$ stem cells can switch their metabolic dependence to fatty acid oxidation (FAO) and glycolytic metabolism depending on availability of specific nutrients and environmental cues.[41−43] Furthermore, distinct, rapidly dividing cell populations with stem-like character are reported to rely on FAO for growth and differentiation,[44] while having the capability to turn up their glycolysis under mitochondrial dysfunction.[45,46] Altogether, this indicates that intestinal stem cells and progenitor cells often show unique metabolic profiles compared to several other adult stem cells and possess a high metabolic plasticity, enabling them to adapt their metabolism to varying environments. This motivates a detailed characterization of the cell metabolism throughout the growth and differentiation of human-derived intestinal organoids.

Received: May 4, 2025
Revised: November 21, 2025
Accepted: November 24, 2025
Published: December 5, 2025

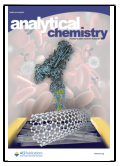

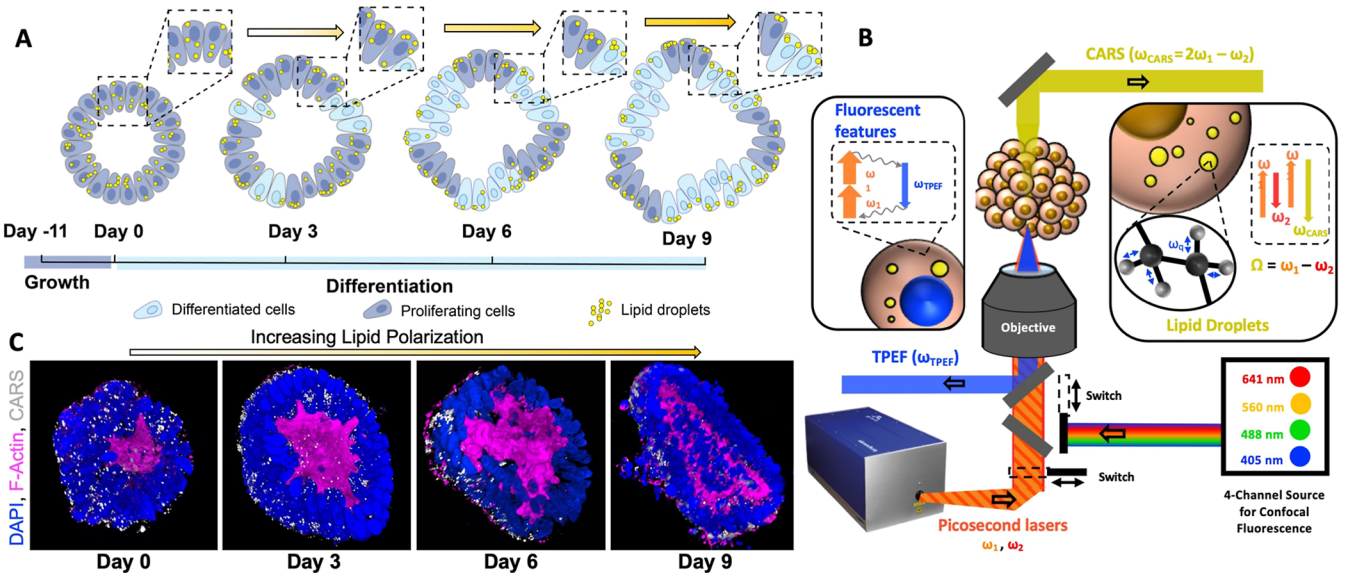

Figure 1. Mapping of LDs in enteroids during differentiation. (A) Schematic of human enteroid differentiation. After 11 days of growth in Matrigel, enteroids were exposed to differentiation medium on day 0. Organoids were collected for immunocytochemistry staining and fluorescence/CARS imaging after differentiation of 0, 3, 6, and 9 days. (B) Schematic of the imaging system combining scanning confocal fluorescence and CARS microscopy. A four-channel excitation source is used for fluorescence imaging, while CARS is excited by two pico-second pulsed excitation beams at frequencies ω_1 and ω_2 that drive Raman-active vibrational modes at the difference frequency, $\Omega = \omega_1 - \omega_2$, yielding a CARS signal at $\omega_{CARS} = 2\omega_1 - \omega_2$. The intracellular LDs are probed at 2850 cm^{-1}, which targets their symmetric methylene stretching vibrations. DAPI (nuclei) signal was obtained by two-photon excited fluorescence (TPEF) in nonlinear images and by confocal fluorescence in linear images to enable channel registry. (C) 3D reconstructions of representative enteroids at the indicated differentiation time points. Over time, the intracellular distributions of LDs become increasingly polarized toward the basal membrane at the periphery of the enteroid.

A prerequisite for such characterization is analytical techniques that can evaluate the identity and state of the cells in parallel with metabolic profiling, ideally with spatial and temporal resolution so that metabolic changes can be correlated with developmental trajectories. For metabolic profiling, assessment of metabolic organelles, such as mitochondria and lipid droplets (LD), can provide insights into the metabolic pathways that dictate the functional states of cells. This is relevant as cell metabolism has been reported to play a pivotal role in regulating a broad range of mammalian stem cell behaviors[34,35,37,38] and metabolites and reactive oxygen species (ROS) act as cofactors in epigenetic control of fate-determining transcriptional programs.[47−50] Techniques to assess the characteristic signatures of intracellular mitochondria and LDs with spatial and temporal precision would enable the assessment of metabolic dynamics in organoids.

Mitochondrial intracellular distributions can be observed through a variety of fluorescent microscopy methods. These techniques have been combined with imaging of LD intracellular distribution using markers with varying levels of specificity.[51,52] It can be combined with imaging of intracellular distributions of LDs using markers with various levels of specificity. BODIPY dyes are a family of fluorescent compounds that spontaneously collect in LDs due to their hydrophobic nature. Dye derivatives have been developed to enable live cell imaging for broad classes of lipids; however, concerns of phototoxicity from generated reactive oxygen species (ROS) have been raised, and their broad emission bands often limit the ability to multiplex with other fluorophores. Furthermore, nonspecific staining of other cellular structures and compartments, such as lysosomes, commonly occurs. A more specific approach is to stain for perilipin proteins that coat LDs; however, such staining often has a high background, in particular when working with organoids embedded in gels.

Coherent anti-Stokes Raman scattering (CARS) microscopy is a strategy that circumvents the issues associated with LD dyes, as it is a completely label-free approach that targets molecular vibrations inherently found in the lipids.[53,54] The high concentration of lipid molecules, which have multiple repeats of methylene groups, provide excellent contrast for LDs when the CH_2 symmetric stretching vibrations are targeted. In addition, qualitative chemical information about the lipid structures can be extracted from CARS data by scanning a complete vibrational spectrum. While molecular specificity at levels that rival lipidomic studies by mass spectrometry cannot be achieved, CARS is a nondestructive approach that is fully compatible with point-scanning microscopes and can readily achieve subcellular spatial resolution with scanning speeds on par with confocal fluorescence imaging.

Here we leverage this virtue in a unique multiplex imaging platform that combines CARS and confocal fluorescence imaging to simultaneously evaluate LDs and mitochondria as key metabolic organelles during the development of human enteroids, defined as epithelial-only intestinal organoids. The LDs were visualized by probing inherent vibrations of C−H_x bonds of lipids using CARS microscopy simultaneously with mitochondria by confocal fluorescence microscopy. The combined LD and mitochondrial mapping was motivated by previous reports demonstrating that their spatial correlation can reveal reliance on mitochondrial oxidation, including FAO and oxidative phosphorylation (OXPHOS).[55−58] We further evaluated the chemical signatures for the LDs by assessing shifts in their methylene vs methyl ratio and degree of lipid unsaturation by analyzing the C−H_x vibrational markers from

https://doi.org/10.1021/acs.analchem.5c02648
Anal. Chem. 2025, 97, 27076−27090

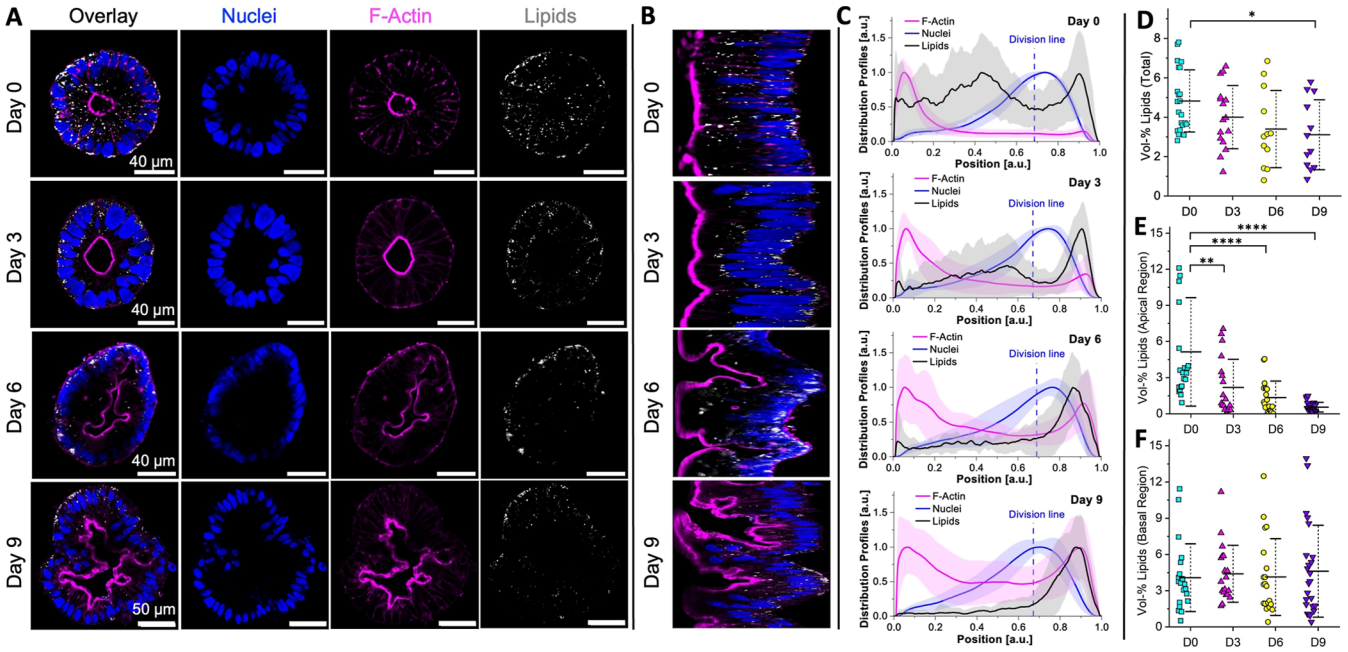

Figure 2. Human enteroid morphology and LD distributions during differentiation. (A) Nuclei (blue), F-actin (magenta) and LDs (CARS, gray) were imaged at 0, 3, 6, and 9 days postdifferentiation. (B) Polar transformed images enable evaluation of radial distributions for the observed features. (C) Distribution profiles for F-actin (magenta), nuclei (blue), and LDs (gray), where solid lines are averages for >13 enteroids and the shaded regions are standard deviations. The distribution of LDs shifts toward the basal side over time, while the central F-actin ring is complemented by a buildup of intracellular actin filaments resulting in a bimodal distribution. The nuclei position remains similar across all time points and is used to define a division line for apical (inner) and basal (outer) features. (D–F) Postdifferentiation, the overall vol % of LDs in the enteroids declines relative to the initial value at Day 0, mainly observed as a reduction in apical LD vol %, while the amount of LDs in the basal region remains unchanged. Each data point represents one enteroid at Day 0 (cyan squares), Day 3 (magenta up-triangles), Day 6 (yellow circles), or Day 9 (purple down-triangles). Statistical evaluations are one-way ANOVA with Tukey's mean tests: *$p < 0.05$, **$p < 0.01$, ****$p < 0.0001$.

CARS spectra. Interestingly, our results revealed a strong spatial polarization of LDs and mitochondria within the enteroids, and an enhanced presence of LDs in cells that also stained positive for markers of proliferation or stemness. This work demonstrates that multiplexed CARS with fluorescence microscopy can readily probe the spatial and temporal dynamics of metabolic cellular processes during human organoid differentiation at the subcellular level. This technology offers new opportunities to quantitatively probe metabolic heterogeneity in multicellular systems. Here, we show that a polarized metabolic and lipid supply infrastructure is formed as an early and important part of the intestinal epithelial differentiation program.

RESULTS

Spatial Mapping of Lipid Droplets in Enteroids During Differentiation. Patient-derived human intestinal enteroids were cultured from single cells embedded in Matrigel and maintained in growth medium for 11 days to allow expansion, after which differentiation was initiated (Figure 1A). Protocols that promote budding formations and controlled balance of intestinal cell fates have recently been developed,[5,6] but are not yet universal and may lead to inconsistent organoid morphologies that pose a challenge for quantitative spatial analyses. Instead, we opted to use commercially available kits for differentiation. Enteroids embedded in the gels were collected, fixed, and stained for imaging after 0, 3, 6, and 9 days of continued growth (controls) or differentiation. Imaging was conducted on a multimodal imaging system, combining scanning confocal fluorescence with nonlinear optical microscopy by switching between different excitation modes, which allowed us to capture fluorescence and CARS signals, respectively (Figure 1B). Apicobasal intracellular distributions of LDs and mitochondria were evaluated during stem cell proliferation and differentiation was assessed by staining for protein markers related to cell proliferation status (Ki67), stemness (BMI1), and mitochondria (Mitotracker Green). Nuclei (DAPI) and F-actin (phalloidin) were also stained to help us track cell morphology and the outline of the enteroids (Figure 1C). Finally, LDs were detected through label-free CARS analysis. We tracked the amounts, spatial distributions, and molecular characteristics of LDs during enteroid development and correlated the results with the organization of the mitochondria, stemness, and proliferation markers.

At Day 0 (i.e., after 11 days of growth), the cells had formed centrosymmetric enteroids, with an F-actin ring in the center and nuclei positioned near the enteroid periphery (Figures 2A, S1, and S2). Consistent with observations by others, upon differentiation using standard human organoid differentiation medium, the F-actin ring expands and then begins to display an undulating internal morphology, while the enteroid periphery showed bud formations.[6,59,60] To map the spatial organization of LDs within the cells, we used the label-free CARS imaging modality to probe the 2850 cm^{-1} vibration, which is strongly represented in LDs due to the methylene groups in their acyl chains.[61] Striking differences in LD organization were observed across different time points (Figure 2A). Before differentiation (Day 0), LDs were homogeneously distributed between the apical and basal membranes. However, following the initiation of differentiation (Days 3, 6, and 9), LDs primarily localized closer to the basal side toward the periphery of the enteroids.

https://doi.org/10.1021/acs.analchem.5c02648
Anal. Chem. 2025, 97, 27076−27090

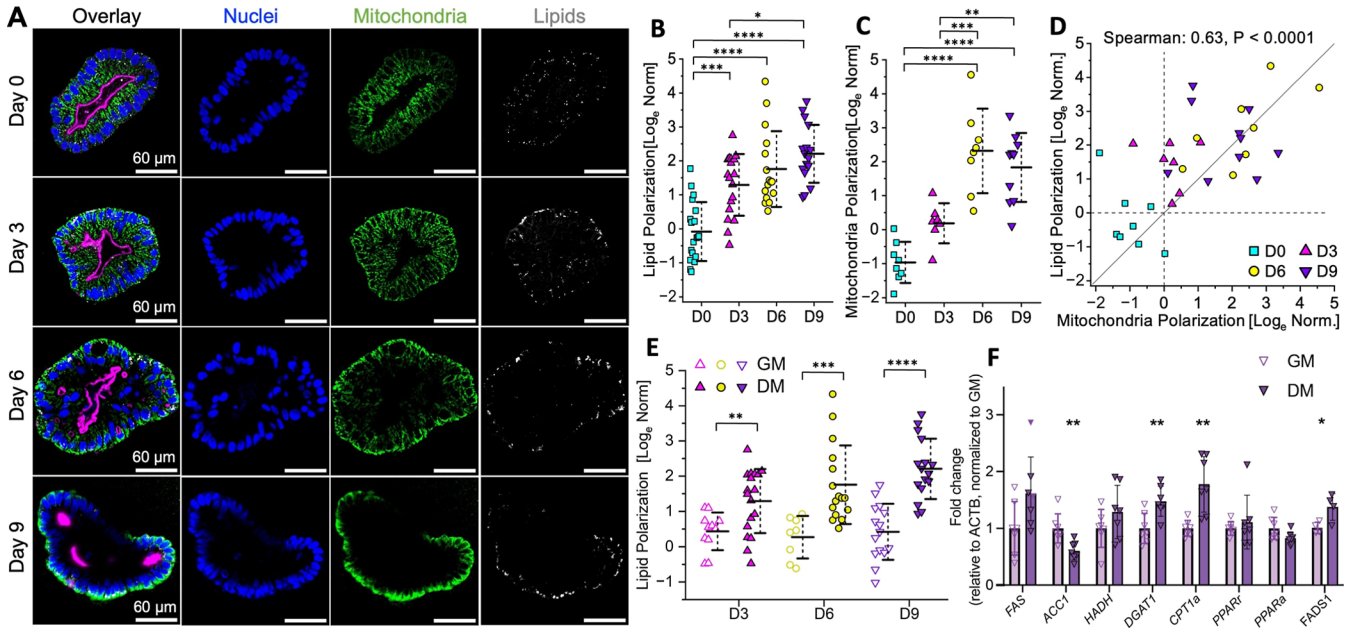

Figure 3. LD and mitochondrial polarization patterns and expression of metabolic regulators. (A) Microscopy images of nuclei (blue), mitochondria (green), and LDs (CARS, gray) indicate that both LDs and mitochondria distributions shift their position in the enteroids postdifferentiation. (B). Log-normalized ratios of LD vol % in the basal region to apical region indicate that the LDs strongly polarize to the basal region over time. (C) Log-normalized ratios of mitochondria vol % in the basal region to apical region indicate that mitochondria are polarized toward the apical region at Day 0, but shift toward the basal region from Day 6 and onward. (D) A correlation plot for the log-normalized polarization ratios indicates that there is strong correlation between LD and mitochondria polarizations (Spearman 0.63, $p < 0.0001$), with the LDs exhibiting earlier polarization toward the basal region as all data points are above the line $y = x$ at Day 3. (E) When comparing enteroids in differentiation medium (DM) with enteroids kept in growth medium (GM) for each time point, the LD polarization is statistically higher in DM. (F) qRT-PCR of lipid metabolic markers at Day 9 postdifferentiation indicates that the enteroids have shifted their gene expression of several metabolic enzymes compared to controls (in GM). Each data point represents one technical replicate, $n = 4–7$. (A–E) Each data point represents one enteroid at Day 0 (cyan squares), Day 3 (magenta up-triangles), Day 6 (yellow circles), or Day 9 (purple down-triangles). Statistical evaluations are one-way ANOVA with Tukey's mean tests (B,C) and Welch's t tests (E,F): $*p < 0.05$, $**p < 0.01$, $***p < 0.001$, $****p < 0.0001$.

The centro-symmetric shape of the enteroids enabled a systematic and quantitative analysis of LD distributions by applying polar transformations to the images, whereby the central apical side of the enteroids was mapped to the left of the polar transformation images and the peripheral basal side to the right (Figure 2B). From the polar transformed images, LD distribution plots were generated (averages of $n > 13$ organoids per time point are shown), where the apical side is set to position 0 and the basal side is set to position 1 (Figure 2C). The distribution plots of the LDs clearly show that, while LDs are organized approximately homogeneously at Day 0, they exhibit an increasingly asymmetric distribution as the differentiation progressed, with a peak near the basal side (at position ∼ 0.9). This asymmetric organization is henceforth referred to as LD polarization.

Concurrently, the central F-actin ring, represented by a strong main peak in the F-actin distribution plot near the apical side at Day 0 (position <0.1), was shaped into an undulating lumen and complemented by a buildup of intracellular F-actin in the enteroid periphery during differentiation. As a result, the F-actin distribution shifted to a broader, bimodal distribution by Day 6 (peaks at ∼0.1 and 0.9). The internal folding of the F-actin is consistent with previous reports.[6,59,60] In contrast, the spatial distribution of nuclei remained approximately the same throughout the different time points (peak value at ∼0.7). This is because the nuclear position is established immediately following cell division as a consequence of actin-dependent cell shape changes (elongation) during enteroid growth, rather than being driven by polarization/differentiation cues.[60,62,63] Leveraging the consistent nuclei positioning, we defined a division line to distinguish between the inside (apical side) and the outside (basal side) regions of the enteroids. The position of the division line was determined by identifying the signal maxima for the nuclei stain. For regions with more than one nuclei due to multiple cell layers, the average position was taken, which explains why the average division lines are sometimes shifted relative to the signal maxima. Further details are provided in the Materials and Methods section and Supporting Information Methods.

We quantified the percentage of enteroid volume (vol %) occupied by LDs and observed a decline from Day 0 to later differentiation time points (Figure 2D). When evaluating this selectively for LDs in the apical region (Figure 2E) and basal region (Figure 2F), we find that this decrease is driven by the depletion of LDs in the apical region, where each successive time point exhibited significantly less LDs. By Day 9, the apical region was almost completely depleted of LDs, while the basal region maintained a LD vol % consistent with the earlier time points. Hence, cells show polarized lipid metabolic profiles associated with cell differentiation, whereby LDs are depleted in the apical region. As the vol % for the peripheral LDs remained consistent, it suggests that the polarization is not due to a net migration of LDs, but rather due to the depletion of existing LDs that are not replenished in the apical region. This implies a distinct need for lipid supply in the apical region throughout cell differentiation and polarization.

The Correlation between Lipid Droplet Polarization and Mitochondria Distribution. To further explore the

https://doi.org/10.1021/acs.analchem.5c02648
Anal. Chem. 2025, 97, 27076−27090

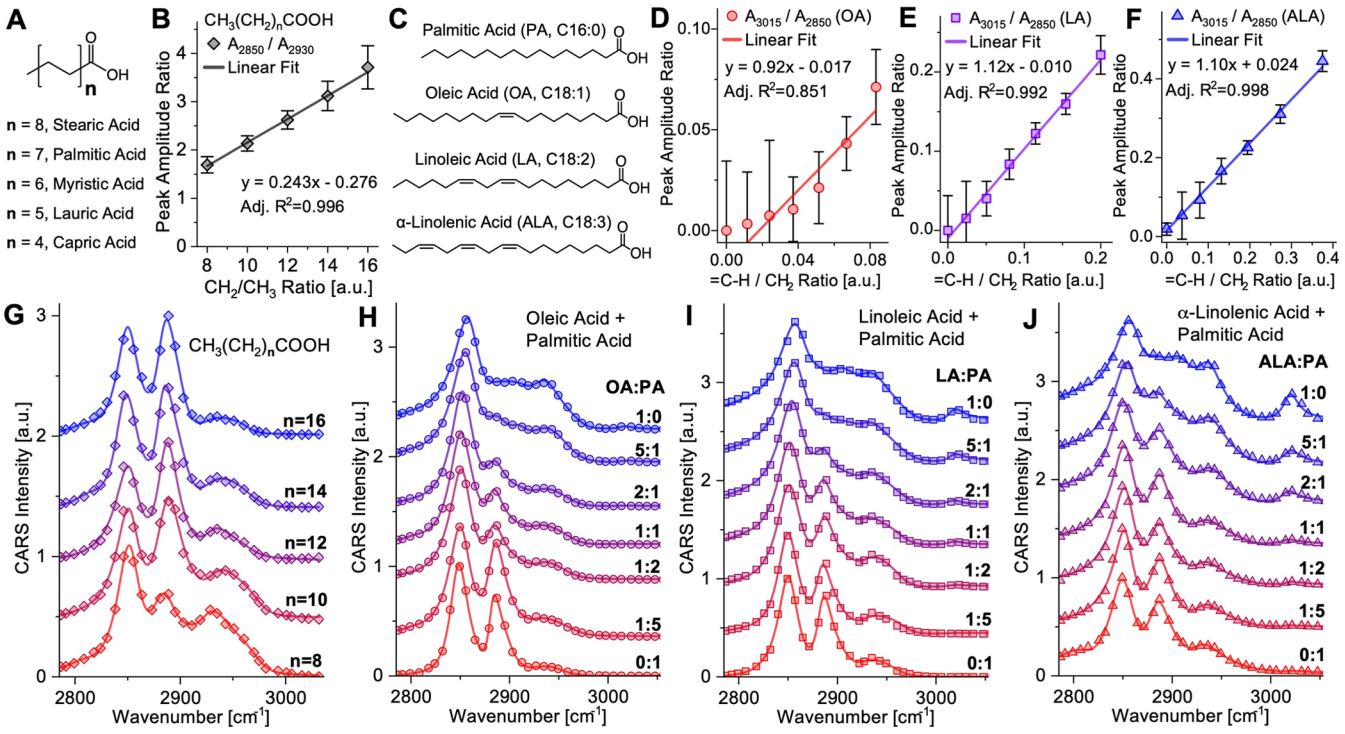

Figure 4. CARS spectral analyses of lipid references. (A) Five saturated fatty acids (C10:0, C12:0, C14:0, C16:0, and C18:0) with different acyl chain lengths were studied; their CARS spectra were collected and analyzed by peak fitting. (B) The peak amplitude ratios for the methylene (2850 cm^{-1}) and methyl (2930 cm^{-1}) stretches were calculated and plotted, indicating a linear relationship vs the acyl chain length (CH_2/CH_3 ratio). (C) A series of saturated (C16:0) and unsaturated (C18:1, C18:2, C18:3) fatty acids were also evaluated. (H-J) Mixtures of the saturated and unsaturated fatty acids with different volume ratios were formed and CARS spectra were measured and analyzed. (D−F) The ratios between the unsaturation (3015 cm^{-1}) and methylene stretching (2850 cm^{-1}) vibrations, were calculated from the fitted parameters and plotted for the various unsaturated lipids, indicating a linear relationship vs the unsaturation rate (=C−H/CH_2 ratio). (G−J) Spectra are shown for the five saturated fatty acids alone and in various mixtures. Symbols are raw data points and solid lines are fits from using eqs 1 and 2. (B,D−F) Symbols are the ratios formed from the fitted peak amplitudes and the solid lines are linear fits for the data vs the known ratios for (B) CH_2/CH_3 or (D−F) =C−H/CH_2. Standard errors from the fits are shown for each ratio data point.

phenomena associated with the lipid polarization, we examined the relative location of mitochondria and LDs, as mitochondria play a crucial role in lipid metabolism by serving as the primary site for fatty acid oxidation, where fatty acids are broken down to generate substrates for cell/organelle membranes and energy in the form of ATP.[64,65] Interactions between mitochondria and LDs indicate local lipid breakdown.[66] To visualize mitochondrial distributions in intestinal enteroids, we stained mitochondria (green) and colocalized them with LDs (Figures 3A, and S3A). Strikingly, the mitochondria displayed a similar trend of polarization toward the basal region during enteroid differentiation. At Day 0 (predifferentiation), most mitochondria were located in the apical region; however, they then gradually shifted in position toward the basal region as differentiation progressed. To evaluate the mitochondrial polarizations over time, we performed a polar transformation of the image stacks and identified a nuclear division line (similar to Figure 2B,C) to quantify the volume % of mitochondria located within the basal region vs the apical region. We then defined a polarization metric that is the log-normalized ratio of the volume % in the basal region to the apical region. In this way, negative values indicated polarization toward the apical region (i.e., ratios less than 1), while positive values indicate polarization toward the basal region (i.e., ratios greater than 1). This polarization metric was also computed for the LD data.

The analysis showed that LD distributions were neutral before differentiation (values near zero), but shifted toward the basal region (positive values) on Day 3 postdifferentiation and increased over time (Figures 3B, and S3B), consistent with the lipid polarization profiles shown previously (Figure 2C). Interestingly, the mitochondria (Figures 3C, and S3C) started off polarized toward the apical region (negative values), shifted to neutral distributions by Day 3 (values near zero), and only became strongly polarized toward the basal region (positive value) at Day 6. Hence, the mitochondrial location correlates well with the observed polarized depletion of LDs. From Day 6, mitochondrial polarization did not increase further (Figures 3A, and S3D). When correlating the LD (y-axis) and mitochondrial (x-axis) polarizations for individual enteroids, the data showed a strong correlation relationship (Spearman parameter = 0.63) (Figure 3D). Importantly, all data points at Day 3 fell above the $y = x$ line, indicating that LDs polarize earlier than mitochondria, hence, that the depletion of the LDs in the apical region is followed by a spatial redistribution of the mitochondria. This observation implies that there is a distinct need for lipid supply in the apical region during early enteroid differentiation that results in a polarized metabolic and lipid supply infrastructure.

We next sought to confirm that the LD and mitochondrial polarization patterns are specifically linked to the differentiation and associated polarization processes, rather than being a manifestation of continued enteroid growth or late-

https://doi.org/10.1021/acs.analchem.5c02648
Anal. Chem. 2025, 97, 27076−27090

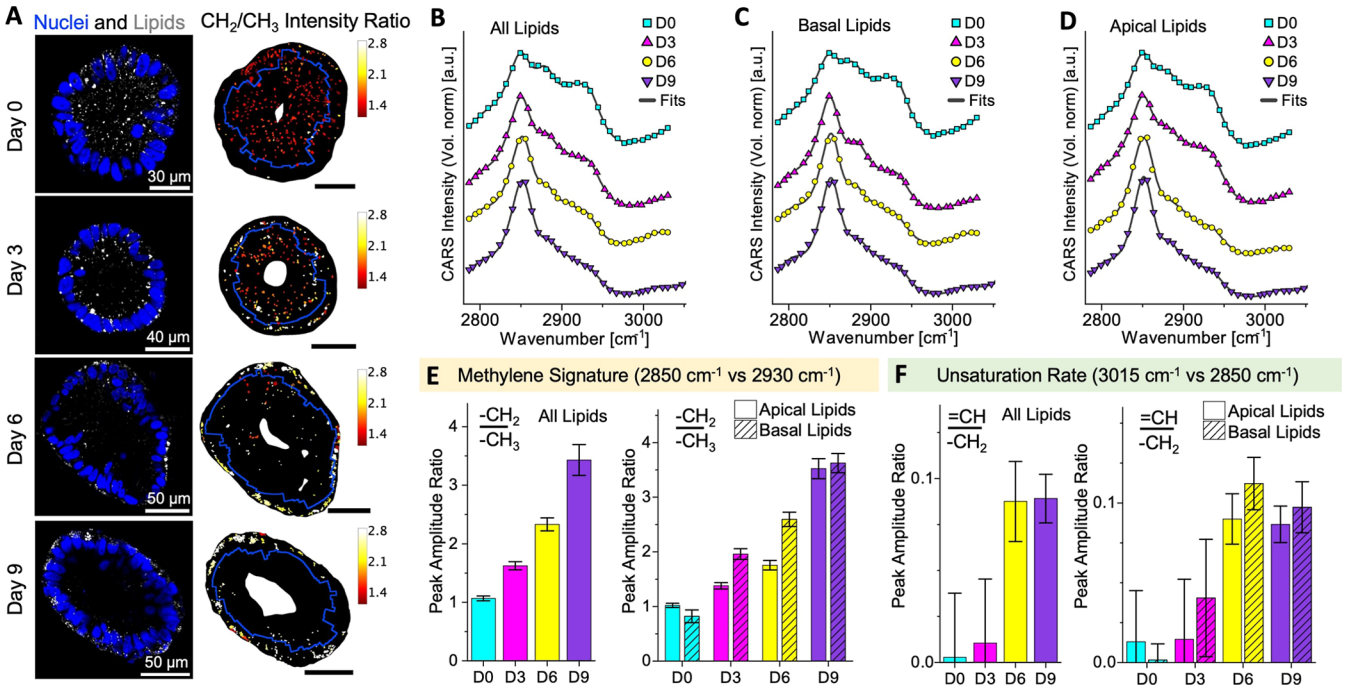

Figure 5. Spatial and temporal dynamics of the chemical composition of LDs. (A) Nuclei/lipid images (left) and corresponding ratio maps (right) of the CARS intensities at vibrations 2850 cm^{-1} and 2930 cm^{-1}, related to the acyl chain length, indicate that there is a shift longer acyl chains postdifferentiation. These lipid droplets can primarily be found in the basal region as determined by the nuclei division line (blue line). (B,C) CARS spectra in the CH_x stretching region for all LDs, basal LDs, and apical LDs at Days 0 (cyan squares), 3 (magenta up-triangles), 6 (yellow circles), and 9 (purple down-triangles). The spectra are fitted (gray lines) using eqs 1 and 2. (E) The peak ratios of the methylene (~2850 cm^{-1}) and methyl (~2930 cm^{-1}) symmetric stretches are calculated from the fits, which indicate an increase in acyl chain length for LDs postdifferentiation. For intermediate time points (Days 3 and 6), LDs in the basal region have longer acyl chains relative to the apical region. (F) Corresponding ratios of the fitted peak parameters for the =C−H stretching vibration (~3015 cm^{-1}) relative to the methylene symmetric stretch (2850 cm^{-1}) suggest an increase in degree of unsaturation postdifferentiation. (E,F) Error bars are standard errors calculated from the uncertainties of the fitted parameters.

stage nutrient deficiency (Figure S1). To test this, we compared the LD polarization in enteroids in differentiation medium with enteroids maintained in growth medium at corresponding time points (Figure 3E). For each time point, LDs remained evenly distributed in the cells of undifferentiated enteroids, in contrast to the high lipid polarization observed for the differentiated enteroids. A slight increase in polarization was observed for enteroids in growth medium at Day 9, which is likely due to spontaneous differentiation known to occur in enteroids at prolonged times.[67]

To investigate possible mechanisms controlling the lipid-related metabolic changes, we performed qRT-PCR to evaluate the expression of lipid-related genes in enteroids 9 days postdifferentiation (Figure 3F, primer information in Table S1). Compared to enteroids cultured in growth medium, differentiated enteroids showed down-regulated expression levels of an indirect beta oxidation inhibitor (*ACC1,* acetyl-CoA carboxylase 1) and up-regulated levels of a fatty acid transporter in the outer mitochondrial membrane (*CPT1a,* carnitine palmitoyltransferase 1a), suggesting an increase in mitochondrial lipid beta oxidation upon cell differentiation. Furthermore, higher expressions of enzymes involved in triglyceride synthesis (*DGAT1,* diacylglycerol-acyltransferase 1) and fatty acid desaturation (*FADS1,* fatty acid desaturase 1) were observed, implying a parallel buildup of unsaturated lipids. Both fatty acid synthase (*FAS*) and the beta-oxdiation related dehydrogenase (*HADH,* hydroxyacyl-CoA dehydrogenase) showed increased expression levels, although the data variability made the shift not statistically significant. Finally, no difference was observed for the transcription factors lipid peroxisome proliferator-activated receptors (*PPARα* and *PPARγ*) that control the overall expression of multiple energy/lipid-related target genes. Together, these results specifically highlight lipid-metabolism related gene expressions and suggest that the cells increasingly rely on mitochondrial respiration supplied by lipid beta oxidation during differentiation, which is consistent with the observed colocalization of LDs and mitochondria that minimizes spatial barriers for mitochondria beta-oxidation. Concomitantly, upregulation of genes critical in lipid synthesis was observed, specifically of unsaturated lipids, indicating a cellular buildup of different categories of lipids in differentiated enteroids. Altogether, this implies that metabolic reprogramming takes place during enteroid differentiation, the downstream results of which are observed as apicobasal redistributions of LDs and mitochondria.

The Chemical Character of the Lipid Droplets Evaluated by CARS Microscopy. Spectral CARS can be used to qualitatively evaluate the type of lipids present in a sample, as the spectral line shape depends on the relative contribution of the vibrational groups inherent in their structure. For saturated long-chain lipids, the high number density of methylene groups gives rise to a strong signal at 2850 cm^{-1}, corresponding to CH_2 symmetric stretching. In contrast, the signal at 2930 cm^{-1}, assigned to CH_3 symmetric stretching, is more pronounced for shorter acyl chains and unsaturated lipids.[53] Thus, the ratio of the CARS peak amplitude at these two wavenumbers (2850 cm^{-1} vs 2930

https://doi.org/10.1021/acs.analchem.5c02648
Anal. Chem. 2025, 97, 27076−27090

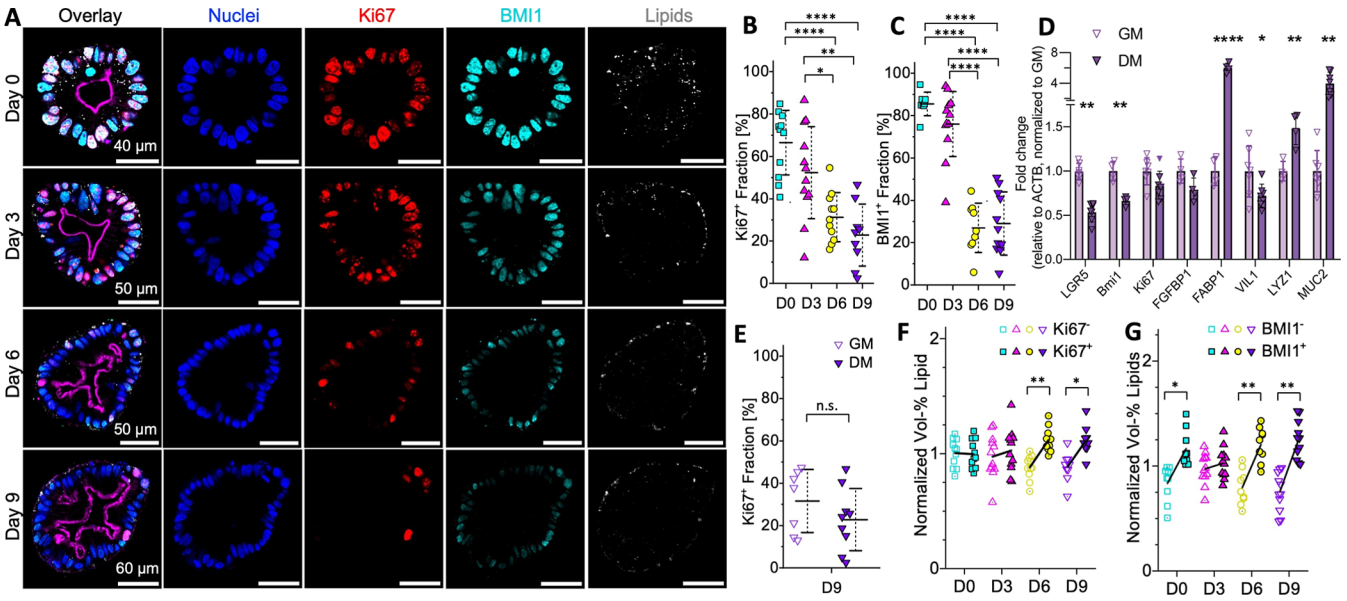

Figure 6. LDs correlate with stem-cell, proliferation, and differentiation status. (A) Enteroids at each time point were stained with proliferation (Ki67, red) and stemness (BMI1, cyan) markers and correlated with LDs (CARS, gray). (B,C) An evaluation of the fraction of cells with Ki67$^+$ or BMI1$^+$ status reveal that the proliferation and stemness of the cells reduce postdifferentiation. (D) qPCR indicates a decline for stemness markers (*LGR5* and *BMI1*), while markers for differentiated intestinal cells (*FABP1*, *LYZ1*, and *MUC2*) increase. (E) Evaluating the Ki67$^+$ fraction for enteroids kept in growth medium (GM, open) does not yield a significant difference from those kept in the differentiation medium (DM, filled). (F-G) At later time points postdifferentiation, the Ki67$^+$ cells have a higher LD vol % than Ki67$^-$ cells (each pair of data normalized to their average). The vol % LDs is higher in general for the BMI1$^+$ cells, although not with statistical significance at Day 3. (B,C,E−G) Each data point represents one enteroid at either, Day 0 (cyan squares), Day 3 (magenta up-triangles), Day 6 (yellow circles), or Day 9 (down-triangles purple). Statistical evaluations are (B,C) one-way ANOVA with Tukey's mean tests, and unpaired (D,E) and paired (F,G) Welch's *t* tests: *$p < 0.05$, **$p < 0.01$, ***$p < 0.001$, ****$p < 0.0001$.

cm^{-1}) is related to the length of saturated acyl-chains for the probed lipids. Furthermore, the peak at 3015 cm^{-1} originates from the stretching vibration of the =C−H group. Accordingly, the unsaturation rate for the lipids can be assessed by a ratio between this peak and the CH_2 stretch vibration (3015 cm^{-1} vs 2850 cm^{-1}). To demonstrate this, we have analyzed peak ratios of lipid standards, which included a series of saturated lipids (Figure 4A,G) with different acyl chain lengths (capric acid, C10,0; lauric acid, C12:0; myristic acid, C14:0; palmitic acid, C16:0; stearic acid, C18:0), as well as unsaturated fatty acids (oleic acid, OA, C18:1; linoleic acid, LA, C18:2; alpha-linolenic acid, ALA, C18:3) that were mixed with a saturated fatty acid (palmitic acid, PA, C16:0) in different ratios (Figure 4C,H−J). We fitted the collected spectra with eqs 1 and 2 (see Materials and Methods) and formed peak ratios between the wavenumbers mentioned above. The results show that the 2850 cm^{-1} vs 2930 cm^{-1} ratio is linearly proportional to the ratio of CH_2 vs CH_3 groups ($y = 0.243x - 0.276$, Adj. $R^2 = 0.996$) in the saturated lipid structures (Figure 4B). Furthermore, the 3015 cm^{-1} vs 2850 cm^{-1} ratio positively correlates with the unsaturation rate in the mixtures, defined by the ratio of =C−H vs CH_2. In the correlation plots, the volume ratios of unsaturated to saturated fatty acids were transformed to a relative ratio of =C−H vs CH_2 based on the molecular structure, weight and relative densities of the fatty acids. For each unsaturated lipid the trends for the amplitude ratios are close to linear (Figure 4D−F), in particular for ALA ($y = 1.10x + 0.024$, Adj. $R^2 = 0.998$) and LA ($y = 1.12x - 0.010$, Adj. $R^2 = 0.992$). For OA, the linear correlation is lower ($y = 0.92x - 0.017$, Adj. $R^2 = 0.851$) as the peak ratios drop rapidly at low unsaturation rates, possibly due to vibrational couplings such as Fermi resonances diminishing the 3015 cm^{-1} peak amplitude.[53] It should also be noted that even pure OA, for which there is one unsaturated bond in each molecule, only exhibits a small peak at 3015 cm^{-1}. Much stronger peak intensities are observed for LA and ALA at 3015 cm^{-1}. This is due to the quadratic dependence on the number density in CARS, which strongly favors vibrational groups with multiple repeats in molecular structures.

To determine whether there are compositional differences in the LDs during enteroid differentiation, as suggested by the gene expression data, we used CARS microscopy to collect vibrational spectra of the LDs and evaluated their relative CH_2 vs CH_3 signatures and the degree of unsaturation. Ratio maps of peaks between 2850 cm^{-1} vs 2930 cm^{-1} for each time point reveal that enteroids accumulate LDs containing acyl chains with stronger methylene signatures postdifferentiation (Figure 5A). At Day 3, LDs in the basal region exhibit a distinct chemical composition compared to LDs in the apical region. This is consistent with our previous result that suggested lipid polarization is not driven by migration of LDs, but rather by the depletion of apical region LDs and replenishment of basal region LDs with newly synthesized lipids. Another important chemical parameter for lipids is the rate of unsaturation. The signal at 3015 cm^{-1} originates from the stretching vibration of unsaturated =C−H groups. However, since the signal is relatively weak, the impact of the nonresonant background, off-resonance water signal, and Fermi resonances of CH_2 deformation overtones make analysis with a simple ratio map challenging.[53] Nevertheless, by collecting complete spectra in the C−H stretching region (Figure 5B−D) and analyzing the data via peak fitting, semiquantitative assessments of both the methylene signature and the unsaturation rate can be achieved, as demonstrated by evaluating the reference lipids above

https://doi.org/10.1021/acs.analchem.5c02648
Anal. Chem. 2025, 97, 27076−27090

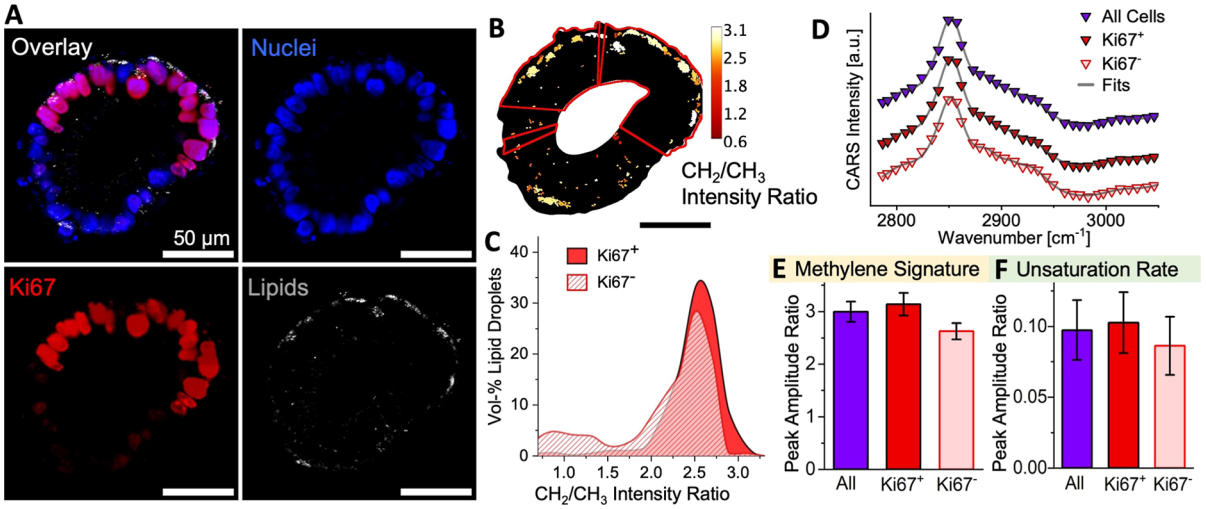

Figure 7. Chemical composition of LDs in proliferating cells in differentiated enteroids. (A) At 9 days postdifferentiation, a subset of cells in the enteroids stain positive for a proliferation marker (Ki67, red), characterized by higher amounts and a polarized distribution of LDs (lipids, gray). (B) The LD acyl chain length ratio map formed between CARS intensities at 2850 cm^{-1} and 2930 cm^{-1} indicates a diverse distribution of ratios, but most of the LDs with high ratios >2.8 are found in the $Ki67^+$ cells. (C) A distribution plot for the methylene vs methyl ratio formed between CARS intensities at 2850 cm^{-1} vs 2930 cm^{-1} shows that ratios associated with short acyl chain length are almost exclusively found in $Ki67^-$ cells and ratios for long acyl chains are more often found in $Ki67^+$ cells. (D) The average CARS spectra of the LDs are shown for all cells (purple), the $Ki67^+$ cells (red), and the $Ki67^-$ cells (pale red) in one enteroid. The spectra show only subtle differences, which are evaluated by peak fitting (dark gray lines) using eqs 1 and 2. (E) The peak ratios of the methylene (~2850 cm^{-1}) and methyl (~2930 cm^{-1}) symmetric stretches are calculated from the fits, which indicate an increase in acyl chain length for $Ki67^+$ cells. (F) Corresponding lipid unsaturation ratios formed between the fitted peak parameters for the =C−H stretching vibration (~3015 cm^{-1}) relative to the methylene symmetric stretch (2850 cm^{-1}). (E-F) Error bars are standard errors calculated from the uncertainties of the fitted parameters.

(Figure 4). The average CARS intensities for all LDs, as well as the those specifically in the apical and basal regions of the enteroids, were extracted and analyzed with eqs 1 and 2 (Materials and Methods).[68] The fitting process converged successfully, and the fitted curves are shown as solid lines (dark gray), which track the data points with high accuracy (Figure 5B−D). From the fits, we extracted quantitative peak ratios (along with their uncertainties derived from the fitted parameters) for the CH_2 vs CH_3 peaks (Figure 5E) and the unsaturation rate (Figure 5F). In both cases, the ratios are increasing with time postdifferentiation. This indicates that the LDs consist of lipids with longer acyl chains and higher rates of unsaturation. The latter conclusion is further supported by increased expression of enzymes involved in fatty acid desaturation (Figure 3F). The ratio between 2850 cm^{-1} and 2930 cm^{-1} is not strictly equivalent to the acyl chain length, since other factors can affect this ratio as well.[1,2] Thus, our conclusion that the acyl chain length is increasing requires further commentary. As shown above (Figure 4E−G), increased saturation enhances the 2850 cm^{-1} peak amplitude, while unsaturation reduces this peak. Hence, saturated lipids with shorter chains can exhibit a higher CH_2 vs CH_3 ratio than longer unsaturated lipids. However, as our data for LDs in intestinal enteroids indicate that the degree of unsaturation is increasing at Days 6 and 9 postdifferentiation, shifts to lower unsaturation cannot explain the observed increase in the 2850 cm^{-1} to 2930 cm^{-1} ratio. With this in mind, our data support the conclusion that there is a shift to longer acyl chains for the LDs postdifferentiation.

When comparing the LDs in the apical region vs the basal region, the basal lipids tend to exhibit signatures of longer acyl chain lengths and higher levels of unsaturation following the initiation of differentiation. However, it should be noted that there were few LDs in the apical region at Day 9 due to the pronounced lipid polarization. Hence, direct comparisons between apical and basal lipids should be made with caution for this time point. Overall, our findings suggest that there is a significant change not only in the amounts and spatial distribution of LDs but also in their chemical composition during enteroid differentiation.

Lipid Droplet Hallmarks vs Cell Proliferation and Differentiation Status. Lipid metabolism is known to play a crucial role in stem cell proliferation and differentiation; proliferating cells have increased de novo lipid synthesis.[38,69] This prompted us to evaluate the enteroid cultures for markers of intestinal stem cells and cell proliferation at several time points (Figure 6A). Specifically, BMI1 is a marker of quiescent intestinal stem cells,[10] while Ki67 is a marker for actively dividing cells.[70] For both markers, the fraction of positive cells was significantly reduced by Days 6 and 9 postdifferentiation, consistent with increasing maturation over time (Figure 6B,C). For Ki67, the fraction of positive cells decreased gradually over time, though most enteroids retained a few strongly Ki67-positive cells indicative of high proliferation, even at Day 9. For BMI1, the fraction of positive cells drastically dropped after Day 3.

At Day 9, we performed qRT-PCR (Figure 6D) to evaluate stem cell markers (*LGR5,* Leucine-rich repeat-containing G-protein-coupled receptor 5; *BMI1,* B cell-specific Moloney murine leukemia virus integration site 1; *FGFBP1,* fibroblast Growth Factor Binding Protein 1), a proliferation marker (*Ki67*), and markers for specialized intestinal epithelial cells including enterocytes (*FABP1,* fatty acid binding protein 1; *VIL1,* villin 1), Paneth cells (*LYZ1,* lysozyme 1), and Goblet cells (*MUC2,* mucin 2). All intestinal cell markers were upregulated in differentiation medium compared to growth medium, with the exception of *VIL1*. *VIL1* is related to the brush border of the microvilli,[71,72] hence, likely minimally

https://doi.org/10.1021/acs.analchem.5c02648
Anal. Chem. 2025, 97, 27076−27090

upregulated as a consequence of the differentiation protocol used that does not promote crypt-villi-like formations in human intestinal organoids.[62,73] Consistent with our microscopy data, qRT-PCR indicated a significant decrease in *BMI1* expression after differentiation. A reduction in *LGR5*, a marker of intestinal stem cells typically located in the crypts,[1,7,8] was also observed. *FGFBP1* decreased as well, but not at a statistically significant level. This gene expression has recently been identified as a marker of a highly proliferating intestinal stem cell population in the transit amplifying region, responsible for replenishing cells both in the villi and crypts of the intestine.[15] Similar to *FGFBP1*, the qRT-PCR data for *Ki67* was trending down upon differentiation, although not at a statistically significant level. This was confirmed by quantitative analysis of the confocal fluorescence images and comparing enteroids in the two media at Day 9 postdifferentiation (Figure 6E), showing a slight but not significant difference in Ki67$^+$ cell fractions. This indicates that cells in both GM and DM are reducing their proliferation over extended culture times (a total of 20 days) as shown for enteroids in DM in Figure 6B, which could be due to spontaneous terminal differentiation that occurs with time. It has been shown that self-renewal maintenance may need niche-specific factors that promote cell proliferation.[3]

We next quantified the LD vol % for Ki67$^+$ vs Ki67$^-$ (Figure 6F) cells and BMI1$^+$ vs BMI1$^-$ cells (Figure 6G) to evaluate if LD presence correlated with stemness and cell proliferation. Overall, both the Ki67$^+$ and the BMI1$^+$ cells showed higher amounts of LDs at the later time points (Day 6 and 9). As previously noted, proliferating cells are known to produce lipids to support their energy needs and formation of additional lipid membranes,[74−76] consistent with our measurements that the Ki67$^+$ cells have more LDs. Since there is a considerable overlap between the BMI1$^+$ cells and the Ki67$^+$ cells as shown by the immunofluorescence images (Figure 6A), the cell proliferation status is likely a contributing factor to the increased amount of LDs observed in BMI1$^+$ cells. Taken together, our results suggest a general trend where LD accumulation in enteroids correlates with both cell proliferation and BMI1$^+$ status. A common, underlying mechanism could be to protect the cells from ROS-induced damage, whereby LDs play a crucial role by sequestering unsaturated lipids to prevent their peroxidation.[77−79]

As the proliferative Ki67$^+$ cell population correlates with higher amounts of LDs, we further evaluated their composition by analyzing the spectral signatures associated with these cells at 9 days postdifferentiation compared to the Ki67$^-$ cells within the same enteroid (Figure 7A). We formed a ratio map between the CARS intensities at 2850 cm^{-1} and 2930 cm^{-1} and found that ratios in a broad range were represented in the enteroid (Figure 7B). While LDs with intermediate ratios (2.0−2.8) are seen throughout the enteroid, the LDs with the highest CH_2 vs CH_3 ratios (>2.8) are almost exclusively found in the Ki67$^+$ cells. In contrast, LDs with low ratios (<2.0) are mostly found in Ki67$^-$ cell populations (Figure 7C). When comparing the CH_x stretching CARS spectra for the LDs in (i) all cells, (ii) the Ki67$^+$ cells, and (iii) the Ki67$^-$ cells, the average spectral differences were subtle (Figure 7D). This conforms with the relatively broad range of CH_2 vs CH_3 ratios observed in the histogram plots for each cell population. In order to quantify these subtle differences, we performed peak fitting of the average CARS spectra using eqs 1 and 2 (Material and Methods) and formed peak ratios from the fitted parameters. This confirmed that the fitted peak ratio between 2850 cm^{-1} and 2930 cm^{-1} was on average higher for the Ki67$^+$ cells compared to the Ki67$^-$ cells, suggestive of lipids with longer acyl chains in the Ki67$^+$ cells (Figure 7E). The lipid unsaturation ratio formed between the fitted CARS intensities at 3015 cm^{-1} and 2850 cm^{-1} indicated an increased degree of unsaturation in the Ki67$^+$ cells compared to the Ki67$^-$ cells, though the uncertainties in the fitted parameters were too large to make a firm conclusion. Nevertheless, these data support the hypothesis that the elevated accumulation of LDs observed in proliferating and stem cells (Figure 7E,F) is a mechanism that protects the cells by sequestering unsaturated lipids, thereby preventing their peroxidation.[77−79]

Interestingly, at early time points (Days 0 and 3) when apically located LDs still dominated, the CARS spectral signatures suggested shorter acyl chains compared to later time points (Figure 5E) despite over 50% of cells being positive for Ki67$^+$ (Figure 6B). However, with increasing formation of basal LDs in the Ki67$^+$ cells (Days 6 and 9), there was a shift in the chemical composition to lipids with longer acyl chains and a higher degree of unsaturation. This trend is supported when analyzing apical and basal LDs separately, consistently showing ratios representing longer acyl chain lipids and a higher degree of unsaturation. Our results suggest that the cells that remain stem-like with Ki67$^+$ status postdifferentiation transfer to a metabolic program that includes the accumulation of basal LDs, sequestering long-acyl chain and unsaturated lipids, possibly to prevent the formation of toxic lipid peroxidation products. Promoting such metabolic shifts and facilitating clearance of lipid peroxides could be a supplemental route to niche-based approaches that improve the long-term self-renewal capacity of human intestinal organoids.[3]

DISCUSSION

Our work combined CARS and confocal fluorescence microscopy to monitor the spatial organization and morphological/compositional changes of LDs and mitochondria during human enteroid differentiation. Our results show that the overall intracellular LD volume decreased during enteroid differentiation, and the distribution of LDs polarize toward the basal membrane over time, which was followed by a correlated mitochondrial polarization. Shifts in the expression of several lipid metabolism markers were observed, suggesting increased triglyceride production and enhanced OXPHOS metabolism in the mitochondria. Spectral CARS analysis of individual LDs indicate that the LDs located near the basal membrane after enteroid differentiation have longer average lipid acyl chain lengths and a moderately enhanced degree of unsaturation. Quantitative evaluations of the unsaturation rate may be performed by probing the C═C vibrations in the fingerprint region,[53] however, nonresonant background signals in this region are often problematic. Stimulated Raman scattering (SRS) may be used to circumvent the impact of nonresonant background signals, however, other types of background need to be properly managed for SRS[80] and an immersion condenser is recommended for improved signal quality.[81] Lipidomic profiling by mass spectrometry for cells sorted by flow cytometry would be another approach to get more detailed insights into the chemical nature of the lipids accumulated in various cells. In combination with CARS and fluorescence microscopy, such information could reveal critical interactions for specific metabolic pathways and programs.

https://doi.org/10.1021/acs.analchem.5c02648
Anal. Chem. 2025, 97, 27076−27090

Finally, we demonstrated that Ki67$^+$ and BMI1$^+$ cells have higher LD vol % than Ki67$^-$ and BMI1$^-$ populations. The LDs in Ki67$^+$ cells further exhibited CARS signatures associated with longer acyl chain lengths and a slightly higher degree of unsaturation, which suggests that their metabolic program includes a protective mechanism whereby these lipids are sequestered in basally located LDs to prevent the formation of toxic peroxidized lipids, hence, supporting long-term cell proliferation. While outside the scope of this investigation, we have observed accumulations of lipid waste outside the enteroid borders with spectral signatures indicative of lower densities of methylene groups, consistent with lipid peroxides. Facilitating the handling of such waste for the organoids may be a strategy to maintain their self-renewal capacity, which would supplement other niche-based approaches and enable studies of conditions and phenomena that only manifest over longer timespans. Taken together, our findings support the idea that substantial cell-type specific lipid metabolic shifts occur during human enteroid differentiation, which manifests in the quantity, chemical composition, and spatial organization of LDs and mitochondria. These findings provide unique insights into the lipid-related processes during enteroid development, which may be leveraged for metabolic control of stem cell function and fate,[50,82] or stimulate novel strategies for improved in vitro maintenance of human enteroids.

One future direction could be to study the hallmarks of LDs in various intestinal stem cell populations. The metabolic signatures of such cells and their progeny are not fully established, partly due to a lack of protocols to characterize stem cell identity in real time. There is ongoing uncertainty on when these multiple stem cell populations coexist, where in the crypt they reside, and to what extent they are active or quiescent during homeostasis and regeneration.[7−9,14] Integrating CARS with techniques like immunocytochemistry (demonstrated in our work here), in situ hybridization (ISH), and other metabolic profiling methods will enable further identification of the metabolic heterogeneity for different stem cell populations. Here, we demonstrate a correlation between BMI1 and LD accumulation, which is consistent with reports that BMI1 has a crucial role in regulating lipid metabolism in several cell types and is correlated with cancer stem cell populations that have been shown to accumulate LDs.[83,84] While antibodies for Lgr5 have been notoriously unreliable for immunofluorescence (thus most work to date on Lgr5$^+$ stem cells are limited to transgenic murine samples), multiplexing of ISH and CARS may offer an opportunity to visualize these stem cell populations in human enteroids in the future.[15]

Similarly, multiplexing CARS with markers of cell proliferation and lineage tracing would offer an opportunity to follow shifts in metabolism during human organoid development. Here, we observed that proliferative Ki67$^+$ cells had an increase in LD accumulation postdifferentiation. Future work to characterize the phenotype of these proliferative cells would be very informative. In particular, evaluating the LD signatures for FGFBP1$^+$ cells and spatially correlating them with Ki67 would be an interesting direction, as the cells that remain highly proliferative (Ki67$^+$ status) may include this recently discovered stem cell population.[15] In murine intestinal epithelium, the highly proliferating Lgr5$^-$ cells in the transit amplifying zone show contrasting metabolic properties relative to other proliferating stem cell types, instead being more similar to that of quiescent stem cells.[41−43] These highly proliferating Lgr5$^-$ cells appear to be flexible in their metabolic pathways, requiring FAO for differentiation while also remaining proliferative upon genetically induced mitochondrial damage,[44] indicating that they can partly rely on glycolysis without mitochondrial respiration.[45,46] Real-time monitoring of such metabolic switches and the dependence on environmental parameters, such as access to nutrients, could be feasible with label-free CARS microscopy.

In our work, we observed polarization of LDs and mitochondria to the basal membrane of enteroids during differentiation. Such polarization, combined with accumulation of debris near the organoid border may affect staining efficiency and imaging depth. However, the fact that nuclear and actin stains were readily probed along with consistent observation of at least a few Ki67$^+$ cells even at Day 9 mitigates such concerns. Furthermore, in the nonlinear imaging, near-infrared excitation light was used, which has long penetration depth and is less impacted by scattering compared to visible light. Since LD polarization was not observed for the enteroids in growth medium, the basal supply of O_2 and nutrients is likely not the main cause. Gobel et al. propose and provide evidence for the formation of a dynamic cytoskeleton in the apical domain of intestinal cells. This cytoskeleton directs vesicle trafficking to deliver apical membrane components independent of the deposition of polarity proteins.[85,86] Since intracellular trafficking and formation of cell membranes require efficient mobilization of energy and supply of lipids, it may result in a polarized metabolic and lipid supply infrastructure as shown here. Apical-basal polarization is commonly observed in spherical, epithelial organoid cultures. Further studies with other epithelial organoids and 2D intestinal cell cultures may elucidate if the LD and mitochondria polarization is a general phenomenon across other culture models with apicobasal features. Future work could also investigate whether flipping the apicobasal polarity of the enteroids, as has been demonstrated for gastrointestinal organoids,[4] alters the LD and mitochondria polarization. In our study, the asymmetric distribution of LDs with long acyl chains, which are the fuel for OXPHOS metabolism and may serve as scavengers of ROS, was observed at earlier time points than mitochondria polarization. This supports the hypothesis that LD polarization could be a driving factor in the spatial reorganization of mitochondria. Future work could test this by inhibiting de novo lipid synthesis[87,88] or disrupting communication between LDs and mitochondria.[89,90]

CONCLUSIONS

In summary, CARS microscopy provides a noninvasive way to spatially, qualitatively, and quantitatively assess lipids in biological samples. As demonstrated here, CARS complements immunocytochemistry techniques by providing spatial information about lipid distribution within cells, enabling the identification of new correlations between lipid composition, cellular localization, and cell phenotype. Traditional mass spectrometry-based metabolomic techniques offer greater sensitivity to chemical diversity; however, these methods typically do not offer cellular-level spatial resolution.[91,92] Thus, CARS microscopy provides a bridge to characterization of smaller length scales, enabling the study of lipid metabolism at the single-cell level with subcellular spatial resolution. When multiplexed with complementary techniques, CARS has the potential to provide a more detailed understanding of metabolic heterogeneity and intracellular processes within

https://doi.org/10.1021/acs.analchem.5c02648
Anal. Chem. 2025, 97, 27076−27090

biological samples. Here we have leveraged these unique capacities and demonstrate the development of a polarized metabolic/lipid-supply infrastructure in human organoid cultures during differentiation, which is accompanied by a shift in chemical character for the lipids as the CARS spectra indicate longer acyl chains and higher unsaturation. These insights may be important for optimizing culture protocols that support long-term self-renewal, in which toxic lipid peroxidation is prevented in the proliferating cell population.

MATERIALS AND METHODS

Human Intestinal Enteroid Passaging and Maintenance Culture. Human enteroids were maintained for ≤21 passages across all experiments. Cells were encapsulated in 40 μL domes of basement membrane extract matrix, specifically Growth factor reduced (GFR) Basement Membrane Matrix (Matrigel) (Corning, Glendale, AZ) within 24-well plates. Organoids were passaged once confluent (∼9−12 days). To remove the organoids from the matrix, Matrigel domes were incubated in prechilled, 5 mM ethylenediamine tetraacetic acid (EDTA) in phosphate buffered saline (PBS) for 30 min and collected and centrifuged for 5 min at 500*g*. Following aspiration of the supernatant, the enteroid pellet was resuspended in Tryp-LE (Thermo Fisher Scientific, Waltham, MA) and incubated at 37 °C for 10 min, with pipet-mixing every 5 min to dissociate the enteroids into single cells. The Tryp-LE was then quenched with enteroid growth media (described below), and centrifuged for 5 min at 500*g*. The quenched solution was then aspirated and the cell pellet was resuspended in fresh media for counting. The pellet was centrifuged one final time at 5 min at 500*g* at the desired cell concentration (750,000 cells/ml for maintenance cultures) and resuspended in prechilled Matrigel. After a 10 min incubation at 37 °C, 700 μL of organoid growth media was added to each well. Small molecule inhibitors, 10 μM Y-27632 and 2.5 μM CHIR99021 (Cayman Chemical, Ann Arbor, MI), were added to the first media change of each maintenance culture. Media was refreshed every 2−4 days, depending on confluence.

Enteroid Growth Media Generation. Enteroid growth media was prepared using a 1:1 mixture of ADMEM/F-12 (Thermo Fisher Scientific, Waltham, MA) with LWRN cell (ATCC CRL3276) conditioned media. Conditioned media was prepared by plating L-WRN cells on T150 f lasks in L-WRN growth media (Dulbecco's Modified Essential Medium DMEM) supplemented with 10% FBS and 1% penicillin-streptomycinglutamine (PSQ). Cells were passaged 2 days after seeding and split at 1:4 ratio. Growth media was replaced with selection media (L-WRN growth medium supplemented with G418 and hygromycin (500 μg/mL)) 1 day after seeding to select for cells expressing Wnt-3A, R-spondin 3, and Noggin. Cells were expanded for 2 additional passages and then cultured with L-WRN collection media (ADMEM/F12 with 10% FBS and 1% PSQ) for 3 days, with media being collected and refreshed every 24 h. Collection media was then mixed in a 1:1 ratio with ADMEM/F-12 and supplemented with the following: 1 mM HEPES (Thermo Fisher Scientific, Waltham, MA), 1× Glutamax (Thermo Fisher Scientific, Waltham, MA), 10 mM nicotinamide (Sigma-Aldrich, St. Louis, MO), 1 mM *N*-acetylcysteine (Sigma-Aldrich, St. Louis, MO), 1× B27 supplement (Thermo Fisher Scientific, Waltham, MA), 0.5 μM A83−01 (Sigma-Aldrich, St. Louis, MO), 1× PSQ (Thermo Fisher Scientific, Waltham, MA), 10 nM Gastrin-I (Sigma-Aldrich, St. Louis, MO), 10 μM SB-202190 (Thermo Fisher Scientific, Waltham, MA), 50 ng/mL recombinant EGF (Thermo Fisher Scientific, Waltham, MA), and 1× Normocin (InvivoGen, San Diego, CA).

Enteroid Differentiation. Human primary intestinal cells were encapsulated in 10 μL (for immunostaining and CARS) of Growth factor reduced (GFR) Basement Membrane Matrix (Matrigel) (Corning, Glendale, AZ) on glass 8-well slides (ibidi Inc., WI, USA) for growth and differentiation. For a period of 11 days, 300 μL of growth media was added to each well for initial enteroid formation and growth. Media was refreshed every 3 days. Following the growth period, each well was treated with 300 μL of IntestiCult Human Organoid Differentiation Medium (STEMCELL Technologies, Vancouver, BC) and 5 μM DAPT (STEMCELL Technologies, Vancouver, BC) for an additional 9 days. Media was refreshed every 2 days for the first 6 days, and every day for the last 3 days. For qRT-PCR, cells were encapsulated in 40 μL Matrigel in a 24-well plate, and 700 μL differentiation media was added and refreshed every 2 days for the first 6 days, and every day for the last 3 days.

Immunocytochemistry. Enteroids cultured for immunostaining were seeded within glass 8-well slides (ibidi Inc.,WI, USA). Cells were fixed with prewarmed 4% paraformaldehyde (PFA) in PBS and incubated at room temperature for 30 min. The PFA was removed and three 10 min PBS washes were completed. Enteroids were permeabilized for 1 h at room temperature with 0.1 wt % digitonin (Thermo Fisher Scientific, Waltham, MA) (PBSD). Enteroids were subsequently blocked with 5% bovine serum albumin (BSA), 5% v/v goat or donkey serum, and 0.1 wt % digitonin in PBS for 3 h on a rocker. Primary antibodies were prepared using the dilutions listed in Table 1 and were diluted with 2.5 wt % BSA, 2.5% v/v goat serum, and 0.1 wt % digitonin in PBS (Antibody Dilution Solution). Enteroids were incubated with primary antibodies overnight at 4 °C. They were then washed with PBS three times, 20 min each. Secondary solutions were diluted at 1:500 in Antibody Dilution Solution and incubated overnight at 4 °C in the dark. Enteroids were again washed with PBS three times, 20 min each. A 1:2000 dilution of DAPI and 1:400 dilution of phalloidin was then prepared and applied to the cells for 2 h. The enteroids were washed with PBS for three additional times, 10 min each. Images were taken using a Stellaris confocal microscope (Leica, Wetzlar, Germany).

Table 1. Primary Antibodies Used for Immunocytochemistry

target	species	vendor	product #	dilution
Ki67	Mouse Mouse	Santa Cruz Biotechnology Cell Signal. Tech	sc-23900 8D5	1:200
Bmi1	Rabbit	Cell Signal. Tech	5856	1:100
Mitochondria	Rabbit Mouse	Cell Signal. Tech. Abcam Inc	COX IV (3E11) [113-1]	1:200

Confocal Fluorescence Microscopy. The stained markers in the cells, as well as the nuclei (DAPI) and F-actin (phalloidin), were imaged by confocal scanning microscopy using an inverted microscope (Nikon, Ti2-E equipped with a C2si$^+$ confocal scanning head and a Nikon CFI Plan Apo IR 60XC water immersion objective, NA = 1.27). The excitation wavelengths (405, 488, 561, and 640 nm) were provided by a 4-channel excitation source (Nikon, LU-

https://doi.org/10.1021/acs.analchem.5c02648
Anal. Chem. 2025, 97, 27076−27090

N4S) and the signals were detected with a tunable emission detector unit (Nikon, C2-DUVB, GaAsP PMT). The four channels were collected sequentially, with a pixel size of <130 nm, a dwell time of 5.5 μs, and a pinhole diameter of 120 μm. For each enteroid, stacks with >15 steps were acquired at a 0.5 μm step size.

Preparation of Lipid Reference Samples. Lipid reference samples were prepared at the bottom of 18-well plates with glass bottom slides (Ibidi). The saturated lipids (capric acid, C10,0; lauric acid, C12:0; myristic acid, C14:0; palmitic acid, C16:0; stearic acid, C18:0) were dissolved in chloroform, and about 20 μL was pipetted into the bottom of the wells. After the chloroform was completely evaporated, a protective layer (~150 μL) of phosphate buffered saline (PBS) was added to the wells. The mixing series of unsaturated lipids (oleic acid, OA, C18:1; linoleic acid, LA, C18:2; alpha-linolenic acid, ALA, C18:3) were prepared by dissolving each lipid individually in chloroform and then mixing them in different ratios with a saturated fatty acid (palmitic acid, PA, C16:0), also dissolved in chloroform. The final ratios of unsaturated and saturated fatty acids were 1:0, 5:1, 2:1, 1:1, 1:2, 1:5, and 0:1. About 20 μL of the mixtures was pipetted into the wells of 18-well glass-bottom plates. For the saturated lipids, the solvent was completely evaporated and a layer of PBS (~150 μL) was added on top. One exception was the pure unsaturated lipids (1:0 ratio), as they were liquid at room temperature. These samples were simply pipetted into the wells 150 μL without a protective layer of buffer. As some phase separation of saturated and unsaturated lipids was seen for the mixtures, large areas (>500 × 500 μm^2) were imaged to minimize the impact on the results.

CARS Microscopy. LDs in the enteroids were mapped by probing CARS signals generated by their CH stretching vibrations in lipids using the confocal fluorescence microscopy platform, complemented by a picosecond (ps)-pulsed laser system consisting of a 1031 nm fiber laser pumping an optical parametric oscillator (OPO) (APE picoEmerald S, 2 ps pulse length, 80 MHz repetition rate, 10 cm^{-1} bandwidth, and tunable between wavelengths 690−960 nm). The fundamental (1031 nm) and tunable laser beams were coupled into the microscope through the microscope scanner, which was equipped with an input module (Optique Peter) that allowed switching between fluorescence and CARS excitation modes. The CH vibrations were coherently driven by the two laser beams overlapped in time and space. To address the methylene symmetric stretching vibrations at 2850 cm^{-1}, which provide high contrast for LDs, the OPO wavelength was set to 797 nm. For a subset of the organoids, we also collected signals from the methyl stretching vibrations at 2930 cm^{-1} by tuning the OPO to 791.8 nm. In both cases, the excitation powers at the sample were 55 mW for the OPO beam and 32 mW for the 1031 nm fundamental beam. The CARS signals were collected in the forward direction using a photomultiplier tube (Hamamatsu, R6357) equipped with hard-coated optical filters (Semrock, one short-pass FF01-750/SP and two bandpass FF01-643/20). The typical dwell time was ~5.5 μs per pixel and the pixel size was <200 nm. To reduce the impact of background signals, we amplitude-modulated the 1031 nm fundamental beam at 20 MHz and isolated the CARS signal with a lock-in-amplifier (Zürich Instruments, HF2LI) synchronized at this modulation frequency. The modulation was primarily performed to remove background from autofluorescence, spontaneous anti-Stokes Raman, and ambient light. For each organoid, stacks with >15 images were acquired with a 0.5 μm distance. For measurements of full spectra in the CH stretching region, we collected sequential stacks while tuning the OPO wavelength between 801 and 784 nm with a step size of 0.5 nm (35 steps in total). To minimize the risk of photodamage, we reduced the excitation powers by ~30% for the spectral acquisitions.

Image Analysis. The acquired images were prepared and analyzed in ImageJ. The CARS images were preprocessed with a Gaussian blur filter (sigma = 1.8) followed by background subtraction with a rolling ball radius of 22 pixels. The preprocessed images were thresholded using the Otsu routine and then manual optimization to ensure that all LDs were included. The outlines of the enteroids were identified by blurring the phalloidin images, manually thresholding them, and filling interior holes that did not represent the lumen area. This allowed us to determine the overall vol % occupied by the LDs by taking the ratio between the volumes of the CARS and phalloidin masks. Masks were also produced for the other markers (Ki67 and BMI1) by applying a Gaussian blur filter (sigma = 5) and enhancing the contrast (~0.1% saturation) for all stack slices to avoid depth-related artifacts, followed by Otsu thresholding. Features below ~25 μm^2 were removed with the Analyze Particles plugin so that only signals representing nuclear markers were included and minor staining artifacts were discarded. The final masks were then dilated three times, to ensure the full width of the cells were typically covered by the masks. The masks and the raw images were then polar transformed from a manually selected point near the center of the organoid with 720 steps, which yielded 0.5 degrees resolution per vertical step in the polar images. These images were then evaluated from the top down in rectangular regions of interest (ROIs) spanning the full width of the phalloidin mask and with a height of 8 lines (4 degrees). If the polar transformed mask for a marker had nonzero values in the ROI, the region was assigned a positive status (value 1) for that marker, otherwise it was assigned a negative status for that marker (value 0). The ROIs were further divided into an inner portion and an outer portion using the x-position for the maximum value of the polar transformed DAPI image as the division line. In this way, masks for the apical region vs the basal region of the enteroids could be constructed, each assigned a status for the stained markers. These constructed masks, as well as the raw data, were then transformed back into Cartesian coordinates and the vol % LDs were evaluated for each region.

For analysis of the spectral scans of images and the making of ratio maps between wavenumbers, we adjusted the thresholding method such that individual LDs could be better separated and individually evaluated. For the stack collected at 2850 cm^{-1}, we used the FindFoci plugin with 1.5 Gaussian blurring, statistics mode both inside and outside, 40 minimum size and 2000 maximum peaks. The background method was St.Dev. above mean (parameter = 1.9), the search method was fraction of peak minus background (parameter = 0.3), and the peak method was relative height (parameter = 0.6). The LDs in the generated masks were then separated with the Disconnect Particles plugin and the resulting mask was used in subsequent analyses, including size evaluation by extracting the LD volumes with the 3D Objects Counter plugin. To evaluate the CARS intensities for the LDs, the average signal within the boundaries for each isolated feature in the mask was determined for each wavenumber using the Intensity Measure-

https://doi.org/10.1021/acs.analchem.5c02648
Anal. Chem. 2025, 97, 27076−27090

ments 2D/3D plugin. From this, spectra for each LD could be extracted. They were further summarized to get an average for each organoid. Furthermore, acyl chain length maps could be produced by forming images where each droplet was assigned the ratio of their average intensities at 2850 cm^{-1} and 2930 cm^{-1}.

Reference Lipids and Lipid Droplet Peak Fitting. The average CARS intensities for all LDs, as well as the those specifically in the apical and basal regions of the enteroids, were extracted and analyzed with eqs 1 and 2 below[68]

$$I_{CARS} = |(\chi_R^{(3)} + \chi_{NR}^{(3)})E_P^2 E_S|^2 \quad (1)$$

$$\chi_R^{(3)} = \sum_q \frac{A_q}{\omega - \omega_q + i\Gamma_q} \quad (2)$$

where E_P and E_S are the E-field strengths of the CARS pump and Stokes beams, respectively. $\chi_{NR}^{(3)}$ represents nonresonant and off-resonant contributions to the nonlinear susceptibility, modeled by a constant, and broad resonances outside of the peak fitting region. Meanwhile, $\chi_R^{(3)}$ represents the resonant contributions, modeled using complex Lorentzian functions shown in eq 2. Each resonant peak is defined by its amplitude (A_q), wavenumber (ω_q), and width (Γ_q). The peak fitting was done using OriginPro and ratios were formed from the fitted amplitudes (A_q) for the peaks at 2850 cm^{-1} vs 2930 cm^{-1} and at 3015 cm^{-1} vs 2850 cm^{-1}.

qRT-PCR. Targeted quantification of mRNA expression was achieved with quantitative reverse transcription polymerase chain reaction. First, to release encapsulated organoids, Matrigel domes were treated with 1 mL prechilled, 5 mM ethylenediamine tetraacetic acid (EDTA) in phosphate buffered saline (PBS) for 30 min and centrifuged for 5 min at 500*g*. The samples were then resuspended in 500 μL of TRIzol reagent (Invitrogen) and immediately transferred to a −80 °C freezer until use. The samples were thawed on ice and disrupted with probe sonication [Heilscher UP50H, 50% amplitude (25 W), 30 kHz frequency, 0.5 s cycle]. mRNA was purified with a phenol-chloroform extraction using 5PRIME phase lock gels (Quantabio) and subsequent isopropyl alcohol precipitation. The mRNA concentration of resuspended solutions was measured with a NanoDrop (Thermo Fisher Scientific), and 100 ng of mRNA was reverse-transcribed per sample with the High-Capacity cDNA Reverse Transcription Kit (Applied Biosystems). The resultant cDNA (6.6 μL) was mixed with 0.9 μL of a 5 μM solution of forward and reverse primer pairs (Integrated DNA Technologies; Table S1) and 7.5 μL of Fast SYBR Green Master Mix (Applied Biosystems). Quantitative polymerase chain reaction was performed with the StepOnePlus Real Time PCR System (Applied Biosystems). Cycle threshold (CT) values were calculated using the StepOnePlus software (v.2.3) and analyzed by the ΔCT method. The primers sequences are in Supporting Information Table S1.

■ ASSOCIATED CONTENT

Supporting Information

The Supporting Information is available free of charge at https://pubs.acs.org/doi/10.1021/acs.analchem.5c02648.

Contains images for enteroid size and morphology change overtime, subcellular lipids and mitochondria distribution, and tables for qPCR primers (PDF)

■ AUTHOR INFORMATION

Corresponding Authors

Sarah C. Heilshorn − *Department of Materials Science and Engineering, Stanford University, Stanford, California 94305, United States;* orcid.org/0000-0002-9801-6304; Email: heilshorn@stanford.edu

Annika Enejder − *Department of Materials Science and Engineering, Stanford University, Stanford, California 94305, United States;* orcid.org/0000-0003-2000-1353; Email: enejder@stanford.edu

Authors

Patrik K. Johansson − *Department of Materials Science and Engineering, Stanford University, Stanford, California 94305, United States*

Yueming Liu − *Department of Materials Science and Engineering, Stanford University, Stanford, California 94305, United States*

Katarina C. Klett − *Institute for Stem Cell Biology and Regenerative Medicine, Stanford University, Stanford, California 94305, United States*

Complete contact information is available at: https://pubs.acs.org/10.1021/acs.analchem.5c02648

Author Contributions

[§]P.K.J. and Y.L. contributed equally. Conceptualization: PKJ, YL, KCK, SCH, AE Methodology: PKJ, YL, KCK, SCH, AE Investigation: PK, YL, KCK Visualization: PK, YL Supervision: SCH, AE Writing—original draft: PKJ, YL, AE Writing—review and editing: KCK, SCH, AE. The manuscript was written through contributions of all authors. All authors have given approval to the final version of the manuscript.

Funding

National Science Foundation Graduate Research Fellowship Program and the National Institutes of Health training grant T32GM119995 (KCK), NSF DMR 2427971 (SCH), NIH R61 CA278450.

Notes

The authors declare no competing financial interest.

■ ACKNOWLEDGMENTS

Research reported in this publication was supported by the National Science Foundation (NSF) Graduate Research Fellowship Program, the National Institutes of Health (NIH) training grant T32GM119995 (K.C.K.), NSF DMR 2427971 (S.C.H.), NIH R61 CA278450 (S.C.H.). Any opinions, findings, and conclusions or recommendations expressed in this material are those of the author(s) and do not necessarily reflect the views of the NSF.

■ ABBREVIATIONS

LDs, lipid droplets; CARS, anti-Stokes Raman scattering; FAO, fatty acid oxidation; OXPHOS, oxidative phosphorylation.

■ REFERENCES

(1) Sato, T.; Stange, D. E.; Ferrante, M.; Vries, R. G.; Van Es, J. H.; Van den Brink, S.; Van Houdt, W. J.; Pronk, A.; Van Gorp, J.; Siersema, P. D.; et al. *Gastroenterology* **2011**, *141* (5), 1762−1772.

(2) Sato, T.; Clevers, H. *Science* **2013**, *340* (6137), 1190−1194.

(3) Fujii, M.; Matano, M.; Toshimitsu, K.; Takano, A.; Mikami, Y.; Nishikori, S.; Sugimoto, S.; Sato, T. *Cell Stem Cell* **2018**, *23* (6), 787−793.

(4) Co, J. Y.; Margalef-Català, M.; Monack, D. M.; Amieva, M. R. *Nat. Protoc.* **2021**, *16* (11), 5171−5192.
(5) Childs, C. J.; Holloway, E. M.; Sweet, C. W.; Tsai, Y. H.; Wu, A.; Vallie, A.; Eiken, M. K.; Capeling, M. M.; Zwick, R. K.; Palikuqi, B.; et al. *JCI Insight* **2023**, *8* (6), No. e165566.
(6) Yang, L.; Wang, X.; Zhou, X.; Chen, H.; Song, S.; Deng, L.; Yao, Y.; Yin, X. *Nat. Commun.* **2025**, *16* (1), 315.
(7) Barker, N.; van Es, J. H.; Kuipers, J.; Kujala, P.; van den Born, M.; Cozijnsen, M.; Haegebarth, A.; Korving, J.; Begthel, H.; Peters, P. J.; et al. *Nature* **2007**, *449* (7165), 1003−1007.
(8) Snippert, H. J.; van der Flier, L. G.; Sato, T.; van Es, J. H.; van den Born, M.; Kroon-Veenboer, C.; Barker, N.; Klein, A. M.; van Rheenen, J.; Simons, B. D.; et al. *Cell* **2010**, *143* (1), 134−144.
(9) Barker, N.; van Oudenaarden, A.; Clevers, H. *Cell Stem Cell* **2012**, *11* (4), 452−460.
(10) Yan, K. S.; Chia, L. A.; Li, X.; Ootani, A.; Su, J.; Lee, J. Y.; Su, N.; Luo, Y.; Heilshorn, S. C.; Amieva, M. R.; et al. *Proc. Natl. Acad. Sci. U.S.A.* **2012**, *109* (2), 466−471.
(11) Ritsma, L.; Ellenbroek, S. I. J.; Zomer, A.; Snippert, H. J.; de Sauvage, F. J.; Simons, B. D.; Clevers, H.; van Rheenen, J. *Nature* **2014**, *507* (7492), 362−365.
(12) Ayyaz, A.; Kumar, S.; Sangiorgi, B.; Ghoshal, B.; Gosio, J.; Ouladan, S.; Fink, M.; Barutcu, S.; Trcka, D.; Shen, J.; et al. *Nature* **2019**, *569* (7754), 121−125.
(13) Beumer, J.; Clevers, H. *Nat. Rev. Mol. Cell Biol.* **2021**, *22* (1), 39−53.
(14) Malagola, E.; Vasciaveo, A.; Ochiai, Y.; Kim, W.; Zheng, B.; Zanella, L.; Wang, A. L. E.; Middelhoff, M.; Nienhüser, H.; Deng, L.; et al. *Cell* **2024**, *187* (12), 3056−3071.
(15) Capdevila, C.; Miller, J.; Cheng, L.; Kornberg, A.; George, J. J.; Lee, H.; Botella, T.; Moon, C. S.; Murray, J. W.; Lam, S.; et al. *Cell* **2024**, *187* (12), 3039−3055.
(16) Huch, M.; Koo, B. K. *Development* **2015**, *142* (18), 3113−3125.
(17) Clevers, H. *Cell* **2016**, *165* (7), 1586−1597.
(18) Bartfeld, S.; Bayram, T.; van de Wetering, M.; Huch, M.; Begthel, H.; Kujala, P.; Vries, R.; Peters, P. J.; Clevers, H. *Gastroenterology* **2015**, *148* (1), 126−136.
(19) Saxena, K.; Blutt, S. E.; Ettayebi, K.; Zeng, X. L.; Broughman, J. R.; Crawford, S. E.; Karandikar, U. C.; Sastri, N. P.; Conner, M. E.; Opekun, A. R.; et al. *J. Virol.* **2016**, *90* (1), 43−56.
(20) Han, X.; Lee, A.; Huang, S.; Gao, J.; Spence, J. R.; Owyang, C. *Gut Microbes* **2019**, *10* (1), 59−76.
(21) Ranganathan, S.; Doucet, M.; Grassel, C. L.; Delaine-Elias, B.; Zachos, N. C.; Barry, E. M. *Infect. Immun.* **2019**, *87* (4), No. e00740.
(22) Koestler, B. J.; Ward, C. M.; Fisher, C. R.; Rajan, A.; Maresso, A. W.; Payne, S. M. *Infect. Immun.* **2019**, *87* (4), No. e00733.
(23) Freire, R.; Ingano, L.; Serena, G.; Cetinbas, M.; Anselmo, A.; Sapone, A.; Sadreyev, R. I.; Fasano, A.; Senger, S. *Sci. Rep.* **2019**, *9* (1), 7029.
(24) Aguilar-Rojas, A.; Olivo-Marin, J. C.; Guillen, N. *Open Biol.* **2020**, *10* (10), 200199.
(25) Sierra, J. C.; Piazuelo, M. B.; Luis, P. B.; Barry, D. P.; Allaman, M. M.; Asim, M.; Sebrell, T. A.; Finley, J. L.; Rose, K. L.; Hill, S.; et al. *Oncogene* **2020**, *39* (22), 4465−4474.
(26) Zang, R.; Castro, M. F. G.; McCune, B. T.; Zeng, Q.; Rothlauf, P. W.; Sonnek, N. M.; Liu, Z.; Brulois, K. F.; Wang, X.; Greenberg, H. B.; et al. *Sci. Immunol.* **2020**, *5* (47), No. eabc3582.
(27) Günther, C.; Winner, B.; Neurath, M. F.; Stappenbeck, T. S. *Gut* **2022**, *71* (9), 1892−1908.
(28) Yan, H. H. N.; Chan, A. S.; Lai, F. P.; Leung, S. Y. *Cell Stem Cell* **2023**, *30* (7), 917−937.
(29) Wang, Q.; Guo, F.; Jin, Y.; Ma, Y. *Signal Transduction Targeted Ther.* **2022**, *7* (1), 336.
(30) Nakamura, T.; Sato, T. *Cell. Mol. Gastroenterol. Hepatol.* **2018**, *5* (1), 51−60.
(31) Kwon, O.; Lee, H.; Jung, J.; Son, Y. S.; Jeon, S.; Yoo, W. D.; Son, N.; Jung, K. B.; Choi, E.; Lee, I. C.; et al. *Nat. Commun.* **2024**, *15* (1), 799.
(32) Hammerhøj, A.; Chakravarti, D.; Sato, T.; Jensen, K. B.; Nielsen, O. H. *iScience* **2024**, *27* (6), 110118.
(33) Rodríguez-Colman, M. J.; Schewe, M.; Meerlo, M.; Stigter, E.; Gerrits, J.; Pras-Raves, M.; Sacchetti, A.; Hornsveld, M.; Oost, K. C.; Snippert, H. J.; et al. *Nature* **2017**, *543* (7645), 424−427.
(34) Folmes, C. D.; Dzeja, P. P.; Nelson, T. J.; Terzic, A. *Cell Stem Cell* **2012**, *11* (5), 596−606.
(35) Shyh-Chang, N.; Ng, H. H. *Genes Dev.* **2017**, *31* (4), 336−346.
(36) Coller, H. A. *FEBS Lett.* **2019**, *593* (20), 2817−2839.
(37) Ly, C. H.; Lynch, G. S.; Ryall, J. G. *Cell Metab.* **2020**, *31* (6), 1052−1067.
(38) Jackson, B. T.; Finley, L. W. S. *Cell Stem Cell* **2024**, *31* (2), 161−180.
(39) Lindeboom, R. G.; van Voorthuijsen, L.; Oost, K. C.; Rodríguez-Colman, M. J.; Luna-Velez, M. V.; Furlan, C.; Baraille, F.; Jansen, P. W.; Ribeiro, A.; Burgering, B. M.; et al. *Mol. Syst. Biol.* **2018**, *14* (6), No. e8227.
(40) Ramalho, S.; Alkan, F.; Prekovic, S.; Jastrzebski, K.; Barberà, E. P.; Hoekman, L.; Altelaar, M.; de Heus, C.; Liv, N.; Rodríguez-Colman, M. J.; et al. *Sci. Adv.* **2025**, *11* (2), No. eadn9750.
(41) Okkelman, I. A.; Neto, N.; Papkovsky, D. B.; Monaghan, M. G.; Dmitriev, R. I. *Redox Biol.* **2020**, *30*, 101420.
(42) Beyaz, S.; Mana, M. D.; Roper, J.; Kedrin, D.; Saadatpour, A.; Hong, S. J.; Bauer-Rowe, K. E.; Xifaras, M. E.; Akkad, A.; Arias, E.; et al. *Nature* **2016**, *531* (7592), 53−58.
(43) Mana, M. D.; Hussey, A. M.; Tzouanas, C. N.; Imada, S.; Barrera Millan, Y.; Bahceci, D.; Saiz, D. R.; Webb, A. T.; Lewis, C. A.; Carmeliet, P.; et al. *Cell Rep.* **2021**, *35* (10), 109212.
(44) Stine, R. R.; Sakers, A. P.; TeSlaa, T.; Kissig, M.; Stine, Z. E.; Kwon, C. W.; Cheng, L.; Lim, H. W.; Kaestner, K. H.; Rabinowitz, J. D.; et al. *Cell Stem Cell* **2019**, *25* (6), 830−845.
(45) Srivillibhuthur, M.; Warder, B. N.; Toke, N. H.; Shah, P. P.; Feng, Q.; Gao, N.; Bonder, E. M.; Verzi, M. P. *Dev. Biol.* **2018**, *439* (2), 92−101.
(46) Li, C.; Zhou, Y.; Wei, R.; Napier, D. L.; Sengoku, T.; Alstott, M. C.; Liu, J.; Wang, C.; Zaytseva, Y. Y.; Weiss, H. L.; et al. *Cell. Mol. Gastroenterol. Hepatol.* **2023**, *15* (4), 931−947.
(47) Perales-Clemente, E.; Folmes, C. D.; Terzic, A. *Antioxid. Redox Signaling* **2014**, *21* (11), 1648−1659.
(48) Tan, D. Q.; Suda, T. *Antioxid. Redox Signaling* **2018**, *29* (2), 149−168.
(49) Schvartzman, J. M.; Thompson, C. B.; Finley, L. W. S. *J. Cell Biol.* **2018**, *217* (7), 2247−2259.
(50) Chandel, N. S.; Jasper, H.; Ho, T. T.; Passegué, E. *Nat. Cell Biol.* **2016**, *18* (8), 823−832.
(51) Mitra, K.; Lippincott-Schwartz, J. *Curr. Protoc. Cell Biol.* **2010**, *4*, 21.
(52) Fu, D.; Mitra, K.; Sengupta, P.; Jarnik, M.; Lippincott-Schwartz, J.; Arias, I. M. *Proc. Natl. Acad. Sci. U.S.A.* **2013**, *110* (18), 7288−7293.
(53) Rinia, H. A.; Burger, K. N. J.; Bonn, M.; Muller, M. *Biophys. J.* **2008**, *95* (10), 4908−4914.
(54) Lee, Y. J.; Vega, S. L.; Patel, P. J.; Aamer, K. A.; Moghe, P. V.; Cicerone, M. T. *Tissue Eng., Part C* **2014**, *20* (7), 562−569.
(55) Cho, Y. M.; Kwon, S.; Pak, Y. K.; Seol, H. W.; Choi, Y. M.; Park, D. J.; Park, K. S.; Lee, H. K. *Biochem. Biophys. Res. Commun.* **2006**, *348* (4), 1472−1478.
(56) Prigione, A.; Fauler, B.; Lurz, R.; Lehrach, H.; Adjaye, J. *Stem Cells* **2010**, *28* (4), 721−733.
(57) Wanet, A.; Arnould, T.; Najimi, M.; Renard, P. *Stem Cells Dev.* **2015**, *24* (17), 1957−1971.
(58) Ludikhuize, M. C.; Meerlo, M.; Gallego, M. P.; Xanthakis, D.; Burgaya Julià, M.; Nguyen, N. T. B.; Brombacher, E. C.; Liv, N.; Maurice, M. M.; Paik, J. H.; et al. *Cell Metab.* **2020**, *32* (5), 889−900.
(59) Hernandez-Gordillo, V.; Kassis, T.; Lampejo, A.; Choi, G.; Gamboa, M. E.; Gnecco, J. S.; Brown, A.; Breault, D. T.; Carrier, R.; Griffith, L. G. *Biomaterials* **2020**, *254*, 120125.

https://doi.org/10.1021/acs.analchem.5c02648
Anal. Chem. 2025, 97, 27076−27090

(60) Hunt, D. R.; Klett, K. C.; Mascharak, S.; Wang, H.; Gong, D.; Lou, J.; Li, X.; Cai, P. C.; Suhar, R. A.; Co, J. Y.; et al. *Adv. Sci.* **2021**, *8* (10), 2004705.
(61) Pezacki, J. P.; Blake, J. A.; Danielson, D. C.; Kennedy, D. C.; Lyn, R. K.; Singaravelu, R. *Nat. Chem. Biol.* **2011**, *7* (3), 137−145.
(62) Klein, J. A.; Heidmann, J. D.; Kiyota, T.; Fullerton, A.; Homan, K. A.; Co, J. Y. *Front. Cell Dev. Biol.* **2025**, *13*, 1508820.
(63) McKinley, K. L.; Stuurman, N.; Royer, L. A.; Schartner, C.; Castillo-Azofeifa, D.; Delling, M.; Klein, O. D.; Vale, R. D. *Elife* **2018**, *7*, No. e36739.
(64) Mayr, J. A. *J. Inherited Metab. Dis.* **2015**, *38* (1), 137−144.
(65) Talari, N. K.; Mattam, U.; Meher, N. K.; Paripati, A. K.; Mahadev, K.; Krishnamoorthy, T.; Sepuri, N. B. V. *Nat. Commun.* **2023**, *14* (1), 766.
(66) Boone, C.; Lewis, S. C. *J. Biol. Chem.* **2024**, *300* (8), 107498.
(67) Thalheim, T.; Quaas, M.; Herberg, M.; Braumann, U. D.; Kerner, C.; Loeffler, M.; Aust, G.; Galle, J. *Dev. Biol.* **2018**, *433* (2), 254−261.
(68) Johansson, P. K.; Schmuser, L.; Castner, D. G. *Top. Catal.* **2018**, *61* (9−11), 1101−1124.
(69) Cruz, A. L. S.; Barreto, E. A.; Fazolini, N. P. B.; Viola, J. P. B.; Bozza, P. T. *Cell Death Dis.* **2020**, *11* (2), 105.
(70) Sun, X.; Kaufman, P. D. *Chromosoma* **2018**, *127* (2), 175−186.
(71) West, A. B.; Isaac, C. A.; Carboni, J. M.; Morrow, J. S.; Mooseker, M. S.; Barwick, K. W. *Gastroenterology* **1988**, *94* (2), 343−352.
(72) Friederich, E.; Vancompernolle, K.; Louvard, D.; Vandekerckhove, J. *J. Biol. Chem.* **1999**, *274* (38), 26751−26760.
(73) Zachos, N. C.; Kovbasnjuk, O.; Foulke-Abel, J.; In, J.; Blutt, S. E.; de Jonge, H. R.; Estes, M. K.; Donowitz, M. *J. Biol. Chem.* **2016**, *291* (8), 3759−3766.
(74) Fernández, L. P.; Gómez de Cedrón, M.; Ramírez de Molina, A. *Front. Oncol.* **2020**, *10*, 577420.
(75) Yao, C. H.; Fowle-Grider, R.; Mahieu, N. G.; Liu, G. Y.; Chen, Y. J.; Wang, R.; Singh, M.; Potter, G. S.; Gross, R. W.; Schaefer, J.; et al. *Cell Chem. Biol.* **2016**, *23* (4), 483−493.
(76) Broadfield, L. A.; Pane, A. A.; Talebi, A.; Swinnen, J. V.; Fendt, S.-M. *Dev. Cell* **2021**, *56* (10), 1363−1393.
(77) Jarc, E.; Kump, A.; Malavašič, P.; Eichmann, T. O.; Zimmermann, R.; Petan, T. *Biochim. Biophys. Acta, Mol. Cell Biol. Lipids* **2018**, *1863* (3), 247−265.
(78) Jarc, E.; Petan, T. *Yale J. Biol. Med.* **2019**, *92* (3), 435−452.
(79) Bailey, A. P.; Koster, G.; Guillermier, C.; Hirst, E. M.; MacRae, J. I.; Lechene, C. P.; Postle, A. D.; Gould, A. P. *Cell* **2015**, *163* (2), 340−353.
(80) Genchi, L.; Laptenok, S.; Liberale, C. *Adv. Phys.: X* **2023**, *8* (1), 2176258.
(81) Yuan, Y.; Lu, F. *J. Vis. Exp.* **2022**.
(82) Ito, K.; Ito, K. *Annu. Rev. Cell Dev. Biol.* **2016**, *32*, 399−409.
(83) Paranjape, A. N.; Balaji, S. A.; Mandal, T.; Krushik, E. V.; Nagaraj, P.; Mukherjee, G.; Rangarajan, A. *BMC Cancer* **2014**, *14*, 785.
(84) Wu, F.; Chen, S.; Ren, S.; Wang, R.; Tan, Y.; Chen, R.; Li, B.; Cao, H.; Li, J. *Recent Pat. Anticancer Drug Discov.* **2025**, *20*, 445.
(85) Jafari, G.; Khan, L. A.; Zhang, H.; Membreno, E.; Yan, S.; Dempsey, G.; Gobel, V. *Sci. Adv.* **2023**, *9* (26), No. eade4022.
(86) Zhang, N.; Zhang, H.; Khan, L. A.; Jafari, G.; Eun, Y.; Membreno, E.; Gobel, V. *Sci. Adv.* **2023**, *9* (26), No. eade4620.
(87) Liu, S.; Lai, J.; Feng, Y.; Zhuo, Y.; Zhang, H.; Chen, Y.; Li, J.; Mei, X.; Zeng, Y.; Su, J.; et al. *J. Biol. Chem.* **2023**, *299* (1), 102720.
(88) Lin, H. P.; Cheng, Z. L.; He, R. Y.; Song, L.; Tian, M. X.; Zhou, L. S.; Groh, B. S.; Liu, W. R.; Ji, M. B.; Ding, C.; et al. *Cancer Res.* **2016**, *76* (23), 6924−6936.
(89) Fan, H.; Tan, Y. *Int. J. Mol. Sci.* **2024**, *25* (13), 6878.
(90) Benador, I. Y.; Veliova, M.; Liesa, M.; Shirihai, O. S. *Cell Metab.* **2019**, *29* (4), 827−835.
(91) Cajka, T.; Fiehn, O. *Anal. Chem.* **2016**, *88* (1), 524−545.
(92) Taylor, M. J.; Lukowski, J. K.; Anderton, C. R. *J. Am. Soc. Mass Spectrom.* **2021**, *32* (4), 872−894.

https://doi.org/10.1021/acs.analchem.5c02648
Anal. Chem. 2025, 97, 27076−27090